Research Square

Preprints are preliminary reports that have not undergone peer review.
They should not be considered conclusive, used to inform clinical practice,
or referenced by the media as validated information.

Present-day ocean circulation constrains divergent overturning futures

Jonathan Baker

jonathan.baker@metoffice.gov.uk

Met Office https://orcid.org/0000-0001-5695-6341

Michael Bell

Met Office

Laura Jackson

UK Met Office https://orcid.org/0000-0003-2326-305X

Geoffrey K Vallis

University of Exeter https://orcid.org/0000-0002-5971-8995

Andrew Watson

University of Exeter https://orcid.org/0000-0002-9654-8147

Richard Wood

Hadley Centre https://orcid.org/0000-0002-3960-9513

Physical Sciences - Article

Keywords:

Posted Date: September 24th, 2026

DOI: https://doi.org/10.21203/rs.3.rs-11045613/v1

License: This work is licensed under a Creative Commons Attribution 4.0 International License.
Read Full License

Additional Declarations: There is **NO** Competing Interest.

Present-day ocean circulation constrains divergent overturning futures

Baker J.A.*[1], Bell M.J.[1], Jackson L.C.[1], Vallis G.K.[2], Watson A.J.[2], Wood R.A.[1]

[1] Met Office, Exeter, UK.

[2] University of Exeter, Exeter, UK.

The Atlantic Meridional Overturning Circulation (AMOC) is projected to weaken, with consequences for climate and ecosystems[1], but its susceptibility to extreme weakening remains uncertain[2,3]. Some recent studies suggest an AMOC tipping point could be crossed by mid-century, potentially committing the circulation to extreme weakening[4–6]. Here, we show that present-day circulation constrains future overturning states. Southern Ocean upwelling predicts models' susceptibility to very weak AMOC states, providing an observational constraint. Our observation-based estimate indicates strong Southern Ocean upwelling, aligning with lower-susceptibility models and suggesting that extreme weakening is unlikely under moderate emissions, even beyond 2100. This implies a lower likelihood of substantial northwestern European cooling associated with an extremely weak AMOC in some simulations[7], although extreme weakening remains possible under stronger forcing. However, lower susceptibility to extreme AMOC weakening does not prevent global overturning reorganisation. Indo-Pacific overturning can reverse before 2100, even under low emissions. Across models, weaker Indo-Pacific return pathways predict greater susceptibility to reversal and a stronger reversed circulation. Our estimate indicates a weak pathway, aligning observations with models more susceptible to this reorganisation and its potential impacts on ocean biogeochemistry and ecosystems[8]. Thus, resilience to extreme AMOC weakening does not imply resilience of the global overturning circulation.

Main

The Atlantic Meridional Overturning Circulation (AMOC) is projected to weaken this century[3,9,10] and may cross a tipping point[2,4,11,12], potentially committing it to subsequent extreme weakening[5,6]. Here, we define an *extremely weak* AMOC state as an AMOC strength below 6 Sv (1 Sv = 10^6 m^3s^{-1}) at 26°N and below 500 m depth (Methods), corresponding to a state often termed AMOC "collapse" or "shutdown"[5,6]; we use *extreme weakening* to refer to reaching this state, avoiding the ambiguity associated with these terms[13]. The AMOC transports heat, nutrients and carbon, and its weakening could substantially affect global climate and marine ecosystems[1,14]. An extremely weak AMOC could intensify some of these impacts and, under moderate global warming, cause substantial cooling in northwestern Europe[7,15]. Yet the wider overturning circulation can reorganise even without extreme AMOC weakening: idealised strong forcing experiments show that changes in deep-water return pathways can reorganise overturning between ocean basins even while the AMOC remains comparatively strong[16,17]. Constraining susceptibility to both extreme AMOC

weakening and broader overturning reorganisation is therefore important for understanding the range of consequences associated with future overturning change[3,8,17].

However, the risks of AMOC tipping and extreme weakening remain highly uncertain, and the two outcomes need not coincide. Climate model projections generally suggest that extreme weakening is unlikely before 2100[3,9,16,18,19], consistent with observational constraints indicating weakening this century but not an extremely weak state[10,20,21]. Meanwhile, statistical estimates[4] and a buoyancy flux indicator[6] suggest that the AMOC is likely to cross a tipping point before 2100, even under moderate emissions. Extended CMIP6 simulations have likewise been interpreted as indicating tipping by mid-century, followed by extreme weakening after 2100 and, in some models, even under low emissions[5]. These contrasting assessments raise a central question: which projected overturning futures are most consistent with the present-day ocean?

One constraint may lie in the pathways through which North Atlantic deep waters return to the surface (AMOC upwelling pathways)[22,23]. The present-day strength of the Indo-Pacific upwelling pathway explains much of the inter-model spread in projected 21st century AMOC weakening[10]. This pathway shuts down in most models, whereas the Southern Ocean (SO) upwelling pathway is more persistent[10,16]. The latter is sustained by wind-driven SO upwelling[24–26]; projected strengthening of SO westerly winds under warming tends to enhance this upwelling[16,27,28], although eddy processes partly offset the response[29]. Under strong forcing, SO upwelling becomes increasingly important as other return pathways weaken[16], suggesting that present-day SO upwelling may predict susceptibility to very weak AMOC states. At the same time, a reversed Indo-Pacific overturning circulation can emerge, redistributing SO upwelling between the Atlantic and Indo-Pacific and reorganising the global overturning circulation without necessarily producing an extremely weak AMOC[16].

Our previous work identified SO upwelling as a mechanism that sustains the AMOC under extreme forcing[16], but whether present-day circulation can discriminate among projected overturning futures remains unknown. Here we show that it can. Across climate models, stronger present-day SO upwelling predicts lower susceptibility to very weak AMOC states, and weaker present-day Indo-Pacific pathways predict stronger future reversed Indo-Pacific overturning and greater susceptibility to its emergence. Observation-based estimates place the present ocean towards models less susceptible to very weak AMOC states but more susceptible to Indo-Pacific reversal.

Estimating present-day overturning pathways

Since SO upwelling cannot be directly observed, we use climate models to train an estimator of SO upwelling from observable ocean properties. We define SO upwelling as the strength of the SO upper overturning cell at 34.5°S and infer the AMOC's Indo-Pacific upwelling pathway from the difference between independently observed AMOC strength and estimated SO upwelling (Methods; Eq. S1–S4). This provides observational estimates of two components of the global return circulation that constrain distinct future overturning responses.

We train a regularised kernel ridge regression across 64 CMIP5 and CMIP6 models (Extended Data Table 1) to estimate present-day SO upwelling from potential density and near-surface temperature at 34.5°S. Leave-one-model-family-out cross-validation tests generalisation across structurally distinct climate models (Methods; Extended Data Fig. 1a). Applying the regression to observations yields our present-day SO upwelling estimate. An independently trained multilayer perceptron neural network gives a similar estimate (Methods; Extended Data Fig. 1b).

Observation-based overturning estimates

Applying the regression to observations over 2005–2024 gives a present-day SO upwelling estimate of 14.3 Sv (10–90% range: 11.4–18.8 Sv; Methods), slightly stronger than the CMIP5/6 ensemble mean of 12.6 Sv. Combined with observed AMOC strength, this implies a weak Indo-Pacific pathway of 3.0 Sv (10–90% range: 0–5.9 Sv; Methods). This range includes uncertainty in SO upwelling; additional systematic uncertainty in South Atlantic overturning is treated separately (Methods), with independent central estimates generally implying a similarly weak Indo-Pacific pathway.

Our SO upwelling estimate is broadly similar to independent observation-based estimates[10] from ECCOv4[30] (14 Sv), an inverse model[31] (11 Sv) and a robust diagnostic simulation[32] (~10.5 Sv). Together with the AMOC estimate, these SO upwelling estimates imply an Indo-Pacific pathway range of 0–6.5 Sv[10], consistent with our observation-based estimate.

SO upwelling constrains susceptibility to very weak AMOC states

We test whether present-day SO upwelling predicts a model's susceptibility – its tendency to reach a very weak AMOC state. We analyse CMIP5/6 simulations under low (RCP2.6/SSP1-2.6), intermediate (RCP4.5/SSP2-4.5), high (RCP6.0/SSP3-7.0) and extreme (RCP8.5/SSP5-

8.5) emissions scenarios, together with idealised abrupt-4xCO2 experiments (hereafter "4xCO2"; Methods). Extended emissions-scenario simulations sample relatively few models and outcomes beyond 2100, whereas 4xCO2 simulations span a wider range of AMOC responses, including models that both reach and avoid very weak states. We therefore use logistic regression across 4xCO2 simulations to quantify how susceptibility varies with control-state SO upwelling (Methods), while emissions scenarios test whether the same association is evident under more realistic forcing pathways. These simulations reveal inter-model differences in susceptibility, not real-world probabilities of reaching very weak AMOC states.

Under 4xCO2 forcing, the AMOC reaches an extremely weak state (<6 Sv at 26°N) within 150 years in 31% (14/45) of models (44% of model families; Extended Data Table 2), although none shuts down completely[16] (orange circles in Fig. 1a and Extended Data Fig. 2a). Susceptibility decreases with stronger control-state SO upwelling across AMOC thresholds from 6 to 9 Sv (Fig. 1a,c and Extended Data Fig. 3a,b). At the 8 Sv threshold, crossed by 21 of 45 models, fitted susceptibility decreases from ~80% to ~20% across the model range ($p < 0.05$; Fig. 1c). At the 6 Sv threshold, the association is similar in direction but less well resolved: fitted susceptibility decreases from ~40% to ~20%, but does not reach statistical significance (Fig. 1a). Similar relationships at 48°N show that the association extends beyond the subtropical AMOC (Fig. 1b,d). Initial AMOC strength is unlikely to account for this relationship: stronger historical AMOCs have been associated with greater subsequent weakening[9], whereas SO pathway strength is not positively correlated with AMOC strength across models[10]. Thus, the lower susceptibility to very weak states associated with stronger SO upwelling is unlikely to arise simply because those models begin with stronger AMOCs.

Our observation-based estimate of present-day SO upwelling (14.3 Sv; 10–90% range: 11.4–18.8 Sv) places the observed ocean towards the lower-susceptibility end of the model distribution. At this upwelling rate, fitted model susceptibility to weakening below 8 Sv is ~30% under 4xCO2 (95% confidence interval: 15–50%), compared with 48% across the full model ensemble (Fig. 1c). Thus, models consistent with observed SO upwelling are less susceptible to reaching very weak AMOC states under 4xCO2.

This association has a physical basis in the AMOC's upwelling pathways. As the Atlantic and Indo-Pacific deep-water return pathways weaken, the AMOC becomes increasingly dependent on its SO pathway. Further AMOC weakening therefore requires this remaining

pathway to weaken, either through reduced SO upwelling or through emergence of a Pacific meridional overturning circulation (PMOC), a reversed Indo-Pacific overturning with sinking predominantly south of the equator[16,17] (Methods). Present-day SO upwelling and the AMOC's SO pathway are nearly identical, but diverge as a PMOC develops: increasing Indo-Pacific sinking diverts more SO upwelling away from the AMOC's SO pathway and into Indo-Pacific overturning[16]. Models with stronger present-day SO upwelling therefore require a larger reduction in SO upwelling or stronger PMOC development for the AMOC to reach a very weak state, explaining their lower susceptibility.

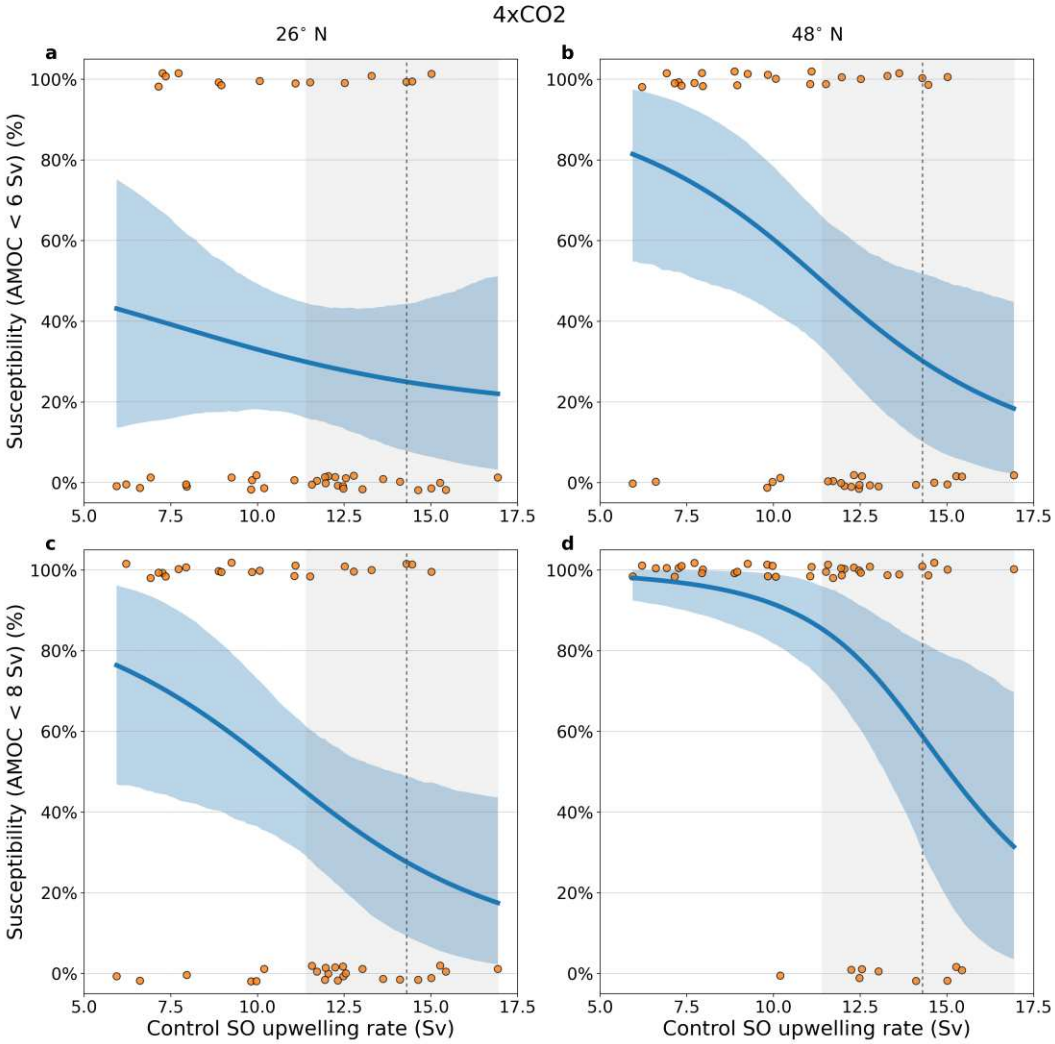

Fig. 1: Susceptibility to very weak AMOC states decreases with stronger present-day Southern Ocean upwelling a–d, Logistic regression estimates of the probability that the AMOC weakens below 6 Sv (extreme weakening) **(a,b)** and 8 Sv **(c,d)** within 150 years of 4xCO2 forcing, as a function of control-state SO upwelling. Results are shown at 26°N **(a,c)** and 48°N **(b,d)**. Orange circles show individual climate model outcomes (100% if the AMOC weakens below the threshold and 0% otherwise; points are vertically offset for visual clarity). Blue lines show fitted probabilities, with shading indicating 95% bootstrap confidence intervals. The dashed

vertical line shows our observation-based estimate of present-day SO upwelling, with grey shading indicating its 10–90% uncertainty range.

Extreme AMOC weakening before 2100 is rare

Relative to 2010, the ensemble-mean AMOC at 26°N weakens by 21%, 26% and 37% by 2100 under SSP126, SSP245 and SSP585, respectively (Fig. 2a,c,e), with similar weakening at 48°N (21–43%). Although weakening increases with emissions, inter-model spread exceeds scenario spread[21,33]. Sensitivity to stronger forcing depends on how far the Atlantic and Indo-Pacific pathways have weakened under SSP126: models in which these pathways are already largely weakened become dominated by the SO pathway and less sensitive to additional forcing, whereas models retaining them remain more sensitive (Extended Data Fig. 4). The Indo-Pacific pathway weakens readily as the AMOC shoals and weakens, with these changes communicated from the Atlantic to the Indo-Pacific through wave processes[22,23,34] (Extended Data Fig. 5b,d,f), whereas the SO pathway is sustained by wind-driven SO upwelling and is therefore more persistent under warming.

Only two of 45 models (CIESM and MRI-ESM2-0) reach an extremely weak AMOC state before 2100 (Fig. 2a,c,e). Both have weak present-day SO upwelling (<9 Sv; Fig. 3a,c,e), consistent with the greater susceptibility associated with weak SO upwelling. CIESM reaches an extremely weak state even under SSP126 and develops one of the strongest PMOCs in the ensemble (4.5–6.5 Sv by 2100; Fig. 3b,d,f), whereas MRI-ESM2-0 reaches this state before 2100 only under SSP585. Thus, both models undergoing extreme weakening this century have present-day SO upwelling well below our observation-based estimate, placing the observed ocean away from the models most susceptible to extreme weakening.

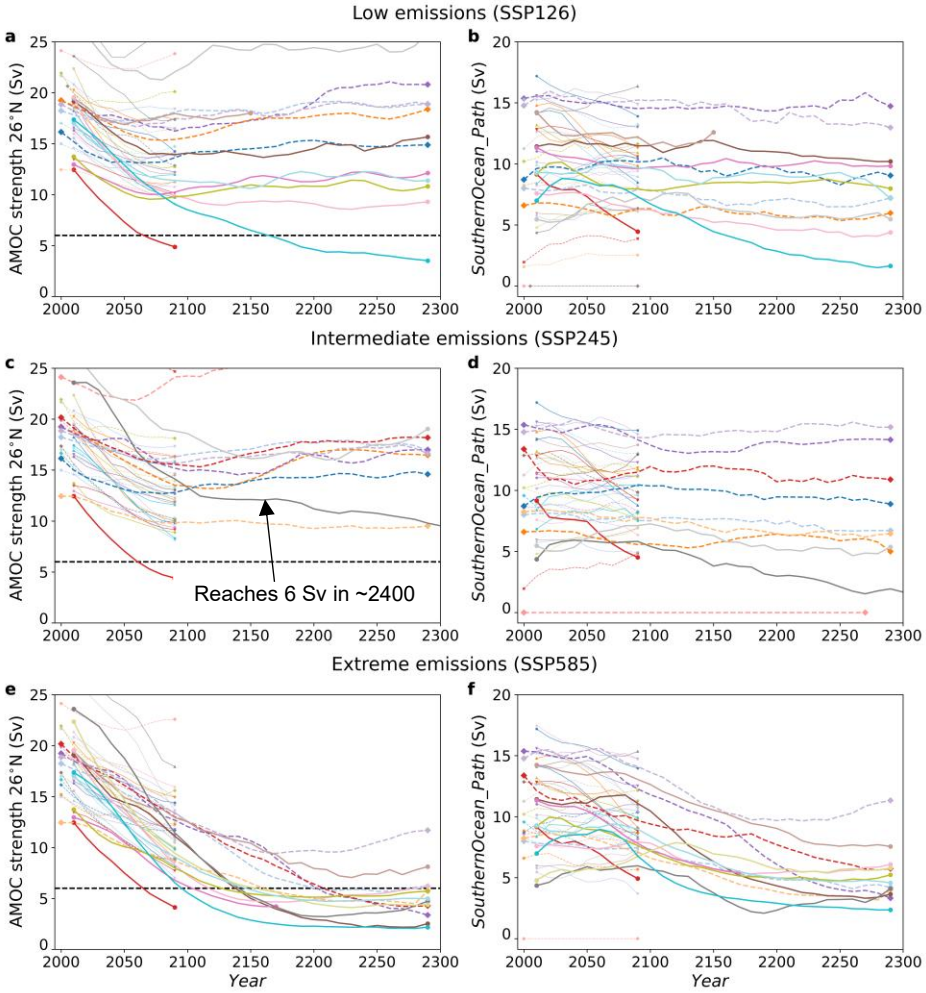

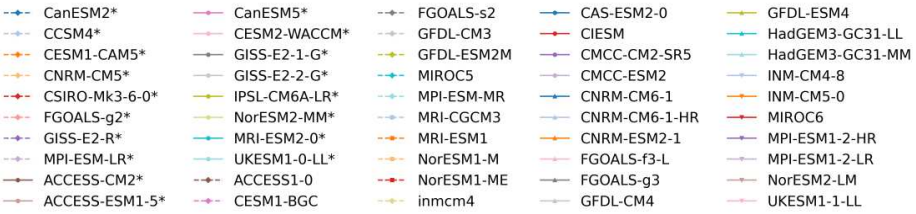

Fig. 2: An extremely weak AMOC state is preceded by weakening of the AMOC's Southern Ocean upwelling pathway. (a-f) AMOC strength at 26°N **(a,c,e)** and its Southern Ocean upwelling pathway ("SouthernOcean_Path") **(b,d,f)**. Rows show low- (SSP1-2.6/RCP2.6) **(a,b)**, intermediate- (SSP2-4.5/RCP4.5) **(c,d)**, and extreme-emissions (SSP5-8.5/RCP8.5) **(e,f)** scenarios. Dashed (solid) coloured lines denote CMIP5 (CMIP6) models, with faint (bold) lines indicating simulations ending in 2100 (2300). The horizontal black dashed line in **(a,c,e)** indicates the 6 Sv extreme-weakening threshold. Models with simulations extended beyond 2100 are labelled with an asterisk. Time series are shown as decadal means and smoothed using a 3-point centred running mean for visual clarity. Note that, in **(c)**, GISS-E2-1-G is shown as not reaching the extreme-weakening threshold because it does so only after 2300. Throughout, analogous SSP and RCP scenarios are grouped under SSP nomenclature; for example, SSP585 includes both SSP5-8.5 and RCP8.5 simulations.

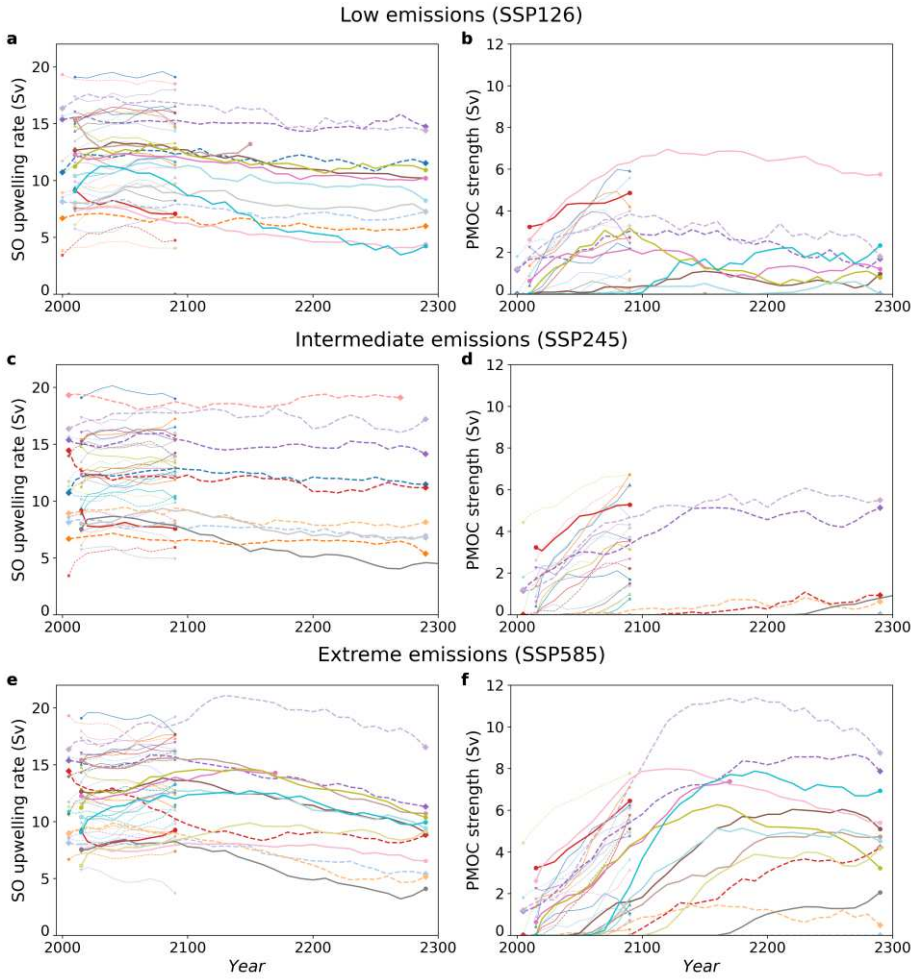

Fig. 3: Changes in Southern Ocean (SO) upwelling and PMOC strength drive changes in the AMOC's Southern Ocean upwelling pathway. a–f, Evolution of the SO upwelling rate (i.e., SO upper cell strength at 34.5°S) **(a,c,e)** and Pacific meridional overturning circulation (PMOC) strength at 34.5°S **(b,d,f)** for low- **(a,b),** intermediate- **(c,d),** and extreme-emissions **(e,f)** scenarios. PMOC trajectories are shown only for models in which a PMOC develops. Dashed (solid) lines denote CMIP5 (CMIP6) models, and faint (bold) lines indicate simulations ending in 2100 (2300). Models with simulations extended beyond 2100 are labelled with an asterisk. Time series are shown as decadal means and smoothed using a 3-point centred running mean for visual clarity.

Extreme weakening beyond 2100 requires a weak SO pathway

Beyond 2100, the AMOC response diverges strongly across emissions scenarios. Extreme weakening at 26°N occurs in 8% (1/12) of models under SSP126 and 10% (1/10) under SSP245, compared with 85% (11/13) under SSP585 (Fig. 2a,c,e and Extended Data Fig. 6a). These fractions should not be interpreted as real-world probabilities because model

availability differs among scenarios and susceptibility to extreme weakening varies across models; rather, the extended simulations reveal the circulation changes associated with extreme weakening. The high incidence under SSP585 occurs under exceptionally strong forcing, with greenhouse-gas concentrations rising well beyond 4xCO2 after 2100 along an increasingly implausible trajectory[35,36].

Under SSP126 and SSP245, the AMOC generally remains above 10 Sv and eventually stabilises or strengthens as the Atlantic and Indo-Pacific pathways recover, while the SO pathway remains sufficiently strong to sustain the circulation (Fig. 2a-d; Extended Data Figs. 5a-d and 7b,c). Under SSP585, most models instead undergo extreme weakening before 2200 as the SO pathway progressively weakens (Fig. 2e,f); the two exceptions have strong present-day SO upwelling (>15 Sv; Fig. 3e).

The AMOC's SO pathway can weaken through two routes: declining SO upwelling or PMOC strengthening, which increases isopycnal downwelling in the Indo-Pacific[17] and diverts SO upwelling away from the AMOC[16]. Although a PMOC develops in 50–92% of models across scenarios (Fig. 3b,d,f), it generally remains weak under SSP126 and SSP245. Under SSP585, however, the PMOC continues to strengthen after 2100, reaching an ensemble mean of ~4.5 Sv by 2200, while SO upwelling itself typically declines by less than ~3 Sv from its present-day strength (Fig. 3e,f). Extreme weakening under SSP585 therefore occurs primarily through continued PMOC strengthening rather than a large decline in wind-driven SO upwelling (Fig. 4).

Only two models reach an extremely weak state beyond 2100 under moderate forcing: MRI-ESM2-0 under SSP126 (Fig. 2a) and GISS-E2-1-G under SSP245, the latter not until around 2400 (not shown). Both maintain weak PMOCs (<2 Sv) but have weak present-day SO upwelling that subsequently declines substantially (Fig. 3a,c), weakening the SO pathway sufficiently even without strong PMOC development (Fig. 4). For GISS-E2-1-G, which shows substantial ensemble spread[37], the AMOC and pathway diagnostics are shown for the ensemble member with the greatest AMOC weakening (Methods). Only 2 of 11 GISS-E2-1-G ensemble members reach an extremely weak state, suggesting an additional role for internal variability[37].

Extreme weakening at 26°N does not imply uniformly weak overturning throughout the Atlantic[16]. Of the 11 SSP585 models that weaken below 6 Sv at 26°N, only 3 also do so at

34.5°S (Extended Data Fig. 7a,d). Extreme weakening therefore reflects a latitudinal reorganisation of the AMOC rather than a uniform shutdown of the circulation[17].

Extreme AMOC weakening thus reflects a common dynamical condition reached through different routes: the AMOC's SO pathway must become sufficiently weak. Under extreme forcing this occurs primarily through PMOC strengthening; in the rare cases under moderate emissions, it occurs through declining SO upwelling in models where present-day SO upwelling is already weak (Fig. 4). Strong present-day SO upwelling therefore reduces susceptibility to extreme weakening, although sufficiently strong forcing can overcome this resilience.

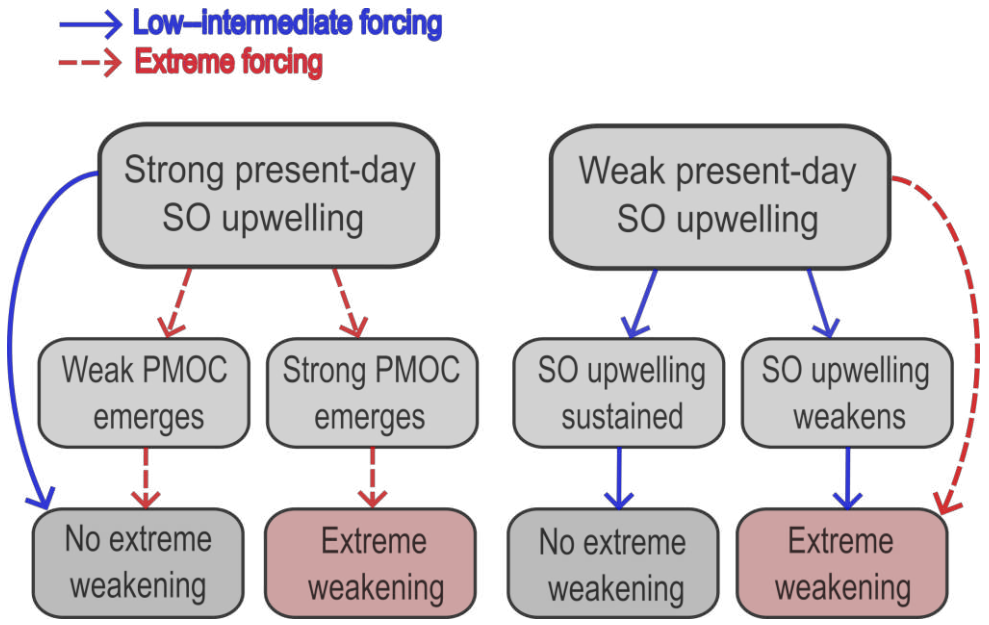

Fig. 4: Extreme AMOC weakening risk after 2100 depends on climate forcing, present-day Southern Ocean upwelling, and the emergent PMOC. Conceptual summary of how the climate forcing, present-day SO upwelling, and the strength of the emergent Pacific meridional overturning circulation (PMOC) determine the risk of extreme AMOC weakening after 2100. Blue and red arrows denote low-to-intermediate (SSP126–SSP245) and extreme (SSP585 or 4xCO2) forcing, respectively.

Mechanisms supporting AMOC resilience

In models undergoing extreme weakening, SO upwelling generally declines (Fig. 3a,c,e) even though SO westerly winds remain at or above their present-day strength and show little latitudinal shift after 2100 (not shown), indicating that weaker winds are not the primary cause. Although wind-driven, the SO upwelling is also influenced by eddy processes and surface buoyancy forcing; the decline may therefore involve reduced SO surface water-mass transformation as surface warming and freshening increase upper-ocean stratification[17].

We hypothesise that strong present-day SO upwelling may also provide thermodynamic support by helping sustain northward heat and salt transport from the tropical to subpolar North Atlantic, thereby supporting North Atlantic sinking and counteracting previously identified destabilising salt-advection and convective feedbacks[5,38]. Consistent with this hypothesis, models with stronger present-day SO upwelling are less susceptible to very weak subpolar overturning at 48°N (Fig. 1b,d). Complete cessation of subpolar sinking remains rare even under strong forcing (Extended Data Figs. 2 and 7). SO upwelling mechanically supports the AMOC by sustaining its SO return pathway and may also enhance thermodynamic resilience. Strong present-day SO upwelling thus increases the forcing required for extreme weakening, helping to explain why this state occurs predominantly under strong forcing or in models with weak present-day SO upwelling (Fig. 4). Susceptibility to extreme AMOC weakening therefore depends not only on North Atlantic processes but also on the state of the global overturning circulation.

Global overturning can reorganise without extreme AMOC weakening

Across emissions scenarios, models with weaker present-day Indo-Pacific pathways develop stronger late-century PMOCs (Fig. 5a-d; $p < 0.05$ across scenarios). This relationship has a physical basis: a strong Indo-Pacific pathway can weaken readily as the AMOC weakens (Extended Data Fig. 5b,d,f), whereas when the pathway is already weak, further AMOC weakening more readily involves reversal of Indo-Pacific overturning, forming a PMOC. The same initial-state dependence emerges under idealised strong forcing: models with weaker control-state Indo-Pacific pathways are more susceptible to developing a PMOC under 4xCO2 (Fig. 5e; $p < 0.05$), with the relationship persisting across a range of thresholds (Extended Data Fig. 3c,d). Stronger control-state SO upwelling is also associated with greater susceptibility to PMOC emergence across a broad range of thresholds (Extended Data Fig. 8), despite being associated with lower susceptibility to very weak AMOC states.

The control-state Indo-Pacific pathway does not, however, provide a similarly robust constraint on susceptibility to very weak AMOC states. Under 4xCO2, its relationship with AMOC threshold crossing is weak, non-significant and differs in direction between the 6- and 8-Sv thresholds ($p > 0.05$; Extended Data Fig. 9a,b). Crossing these thresholds among models with weak Indo-Pacific pathways partly reflects weaker initial AMOCs and stronger PMOC development, whereas some models with strong Indo-Pacific pathways cross where control-state SO upwelling is weak (Extended Data Fig. 9c). Thus, the Indo-Pacific pathway better

predicts future PMOC development, whereas SO upwelling provides the more robust constraint on susceptibility to very weak AMOC states.

Reversed Indo-Pacific overturning can emerge well before 2100, including under low emissions (Fig. 3b,d,f and Extended Data Fig. 6f). By 2100, PMOCs stronger than 3 Sv develop in ~25% of models under SSP126 and ~40% under SSP245 and SSP585 (Fig. 3b,d,f). This reversal diverts part of the SO upwelling into the Indo-Pacific[16] and can therefore substantially alter global overturning while the AMOC remains well above the extreme-weakening threshold (Fig. 2a,c,e and Fig. 3b,d,f).

Our observation-based estimate indicates a weak present-day Indo-Pacific pathway of ~3 Sv, placing the observed ocean towards models that develop stronger future PMOCs across emissions scenarios and are more susceptible to PMOC emergence under 4xCO2 (Fig. 5). Because the Indo-Pacific pathway weakens readily as the AMOC weakens[22,23,34], continued AMOC weakening[39] could further diminish its contribution to the return circulation. PMOCs often emerge before the pathway disappears entirely and, where extreme AMOC weakening occurs, well before the AMOC reaches such a state (Figs. 2a,c,e and 3b,d,f; Extended Data Fig. 5b,d,f). Whether these conditions lead to a persistent PMOC in the observed ocean remains uncertain.

Such reorganisation could alter exchanges of heat, carbon and nutrients between the deep and upper ocean, with implications for ocean heat uptake[40], biogeochemical cycling[8] and marine ecosystems. The weak observed Indo-Pacific pathway therefore suggests that the present ocean may be susceptible to substantial global overturning reorganisation even without the AMOC reaching an extremely weak state.

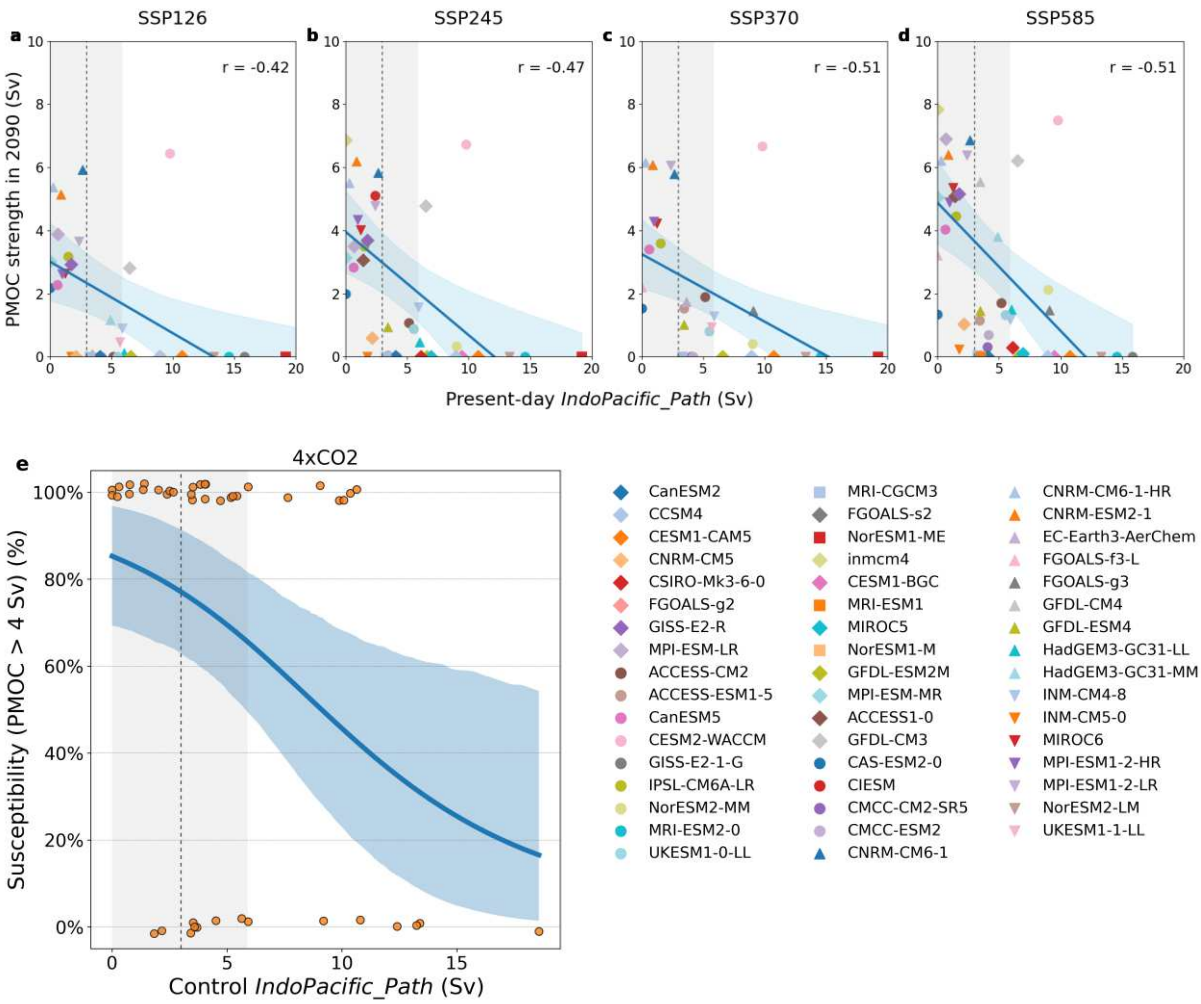

Fig. 5: Weak present-day Indo-Pacific pathway predicts stronger future PMOC development. a-d, Relationship between the AMOC's present-day Indo-Pacific upwelling pathway and PMOC strength in 2090 across CMIP5 and CMIP6 models under low- (SSP1-2.6/RCP2.6) **(a)**, intermediate- (SSP2-4.5/RCP4.5) **(b)**, high- (SSP3-7.0/RCP6.0) **(c)**, and extreme- (SSP5-8.5/RCP8.5) **(d)** emissions scenarios. **(e)** Logistic regression estimate of the probability that the PMOC exceeds 4 Sv within 150 years of abrupt-4xCO2 forcing as a function of control-state Indo-Pacific pathway strength. Points show individual climate model outcomes (100% if the PMOC exceeds 4 Sv and 0% otherwise; vertically offset for clarity), the blue line shows the fitted probability and shading indicates the 95% bootstrap confidence interval. The relationship is robust across a range of PMOC thresholds (Extended Data Fig. 3c,d). In all panels, the dashed vertical line shows our observation-based estimate of the present-day Indo-Pacific pathway, with grey shading indicating its 10–90% range arising from uncertainty in the SO upwelling estimate. Diamonds/squares (circles/triangles) represent CMIP5 (CMIP6) models.

Implications for future overturning

Our results provide an observation-based constraint on susceptibility to extreme AMOC weakening, informing the interpretation of divergent recent assessments. Models with stronger present-day SO upwelling are less susceptible to very weak AMOC states, whereas those reaching an extremely weak state under moderate forcing have SO upwelling weaker than multiple observation-based estimates. Extreme AMOC weakening under moderate

emissions therefore appears less likely than suggested by some recent studies[5,6], although sufficiently strong forcing can overcome this resilience.

This constraint applies to reaching an extremely weak AMOC state rather than directly to tipping. Some recent studies interpret transitions to an extremely weak AMOC state as being preceded by tipping[5,6,12] and suggest that such tipping could occur before 2100[4–6]. Yet extreme weakening remains uncommon under SSP245 even as warming reaches 3.3°C (2.3–4.6°C) by 2300[3], and most models avoid it under 4xCO2 (Extended Data Fig. 2a) despite ~6°C (4–12°C) warming after 150 years[41], by which time many AMOCs stabilise or begin to strengthen[16]. Longer simulations show that the AMOC can subsequently strengthen above 6 Sv after weakening below this threshold under sustained 4xCO2 forcing[42], indicating that the 6 Sv threshold alone does not diagnose tipping. Together with the observational constraint, these results do not determine whether tipping occurs, but provide little support for scenarios in which tipping this century under moderate emissions commits the circulation to subsequent extreme weakening. This in turn reduces the likelihood of substantial northwestern European cooling associated with an extremely weak AMOC in some simulations[7].

Important uncertainties remain. Freshwater forcing biases could cause models to underestimate susceptibility to extreme weakening[43], although realistic meltwater forcing may have limited effects under moderate emissions[44]. Other structural biases can amplify[12,21,45] or suppress projected weakening[9,10,20], while abrupt-4xCO2 forcing may overestimate susceptibility relative to gradual forcing[46,47]. Internal variability can also trigger transitions under moderate forcing, as in some GISS-E2-1-G ensemble members under SSP245[37]; notably, this model has weak present-day SO upwelling. This raises the possibility that stronger SO upwelling may also enhance resilience to noise-induced transitions by increasing the perturbation required to reach a very weak state. Despite these uncertainties, our constraint complements previous observation-based constraints from present-day AMOC strength[9,20] and the AMOC's Indo-Pacific pathway[10], together indicating that the most severe AMOC responses under moderate forcing are less consistent with the observed ocean.

Extreme AMOC weakening and broader overturning reorganisation emerge as two distinct future risks. Present-day circulation places the observed ocean away from models most susceptible to extreme AMOC weakening, while its weak Indo-Pacific pathway is associated with greater susceptibility to reversed Indo-Pacific overturning. Avoiding an extremely weak AMOC does not prevent substantial reorganisation of the global overturning circulation, with

potential consequences for ocean heat transport, biogeochemistry and ecosystems. Present-day observations therefore distinguish among projected overturning trajectories, constraining susceptibility to both extreme AMOC weakening and global overturning reorganisation.

Refereneces

1. Bellomo, K., Angeloni, M., Corti, S. & von Hardenberg, J. Future climate change shaped by inter-model differences in Atlantic meridional overturning circulation response. *Nat. Commun. 2021 121* **12**, 1–10 (2021).
2. Armstrong McKay, D. I. *et al.* Exceeding 1.5°C global warming could trigger multiple climate tipping points. *Science* **377**, eabn7950 (2022).
3. Intergovernmental Panel on Climate Change (IPCC). *Climate Change 2021 – The Physical Science Basis: Working Group I Contribution to the Sixth Assessment Report of the Intergovernmental Panel on Climate Change*. (Cambridge University Press, Cambridge, 2021). doi:10.1017/9781009157896.
4. Ditlevsen, P. & Ditlevsen, S. Warning of a forthcoming collapse of the Atlantic meridional overturning circulation. *Nat. Commun. 2023 141* **14**, 1–12 (2023).
5. Drijfhout, S., Angevaare, J. R., Mecking, J., van Westen, R. M. & Rahmstorf, S. Shutdown of northern Atlantic overturning after 2100 following deep mixing collapse in CMIP6 projections. *Environ. Res. Lett.* **20**, 094062 (2025).
6. van Westen, R. M., Vanderborght, E., Kliphuis, M. & Dijkstra, H. A. Physics-Based Indicators for the Onset of an AMOC Collapse Under Climate Change. *J. Geophys. Res. Oceans* **130**, e2025JC022651 (2025).
7. van Westen, R. M. & Baatsen, M. L. J. European Temperature Extremes Under Different AMOC Scenarios in the Community Earth System Model. *Geophys. Res. Lett.* **52**, e2025GL114611 (2025).
8. Sun, S., Thompson, A. F., Yu, J. & Wu, L. Transient overturning changes cause an upper-ocean nutrient decline in a warming climate. *Nat. Commun.* **15**, 7727 (2024).

9. Weijer, W., Cheng, W., Garuba, O. A., Hu, A. & Nadiga, B. T. CMIP6 Models Predict Significant 21st Century Decline of the Atlantic Meridional Overturning Circulation. *Geophys. Res. Lett.* **47**, e2019GL086075 (2020).

10. Baker, J. A. *et al.* Overturning Pathways Control AMOC Weakening in CMIP6 Models. *Geophys. Res. Lett.* **50**, e2023GL103381 (2023).

11. Boers, N. Observation-based early-warning signals for a collapse of the Atlantic Meridional Overturning Circulation. *Nat. Clim. Change 2021 118* **11**, 680–688 (2021).

12. Westen, R. M. van, Kliphuis, M. & Dijkstra, H. A. Physics-based early warning signal shows that AMOC is on tipping course. *Sci. Adv.* **10**, 1189 (2024).

13. Macneill, K., Martin, L., Wood, R. A. & Sutton, R. An Up-HILL Battle: Towards clearer terminology for High-Impact Climate Possibilities, including tipping points. *EGUsphere* 1–37 (2026) doi:10.5194/egusphere-2026-3767.

14. Liu, W., Fedorov, A. V., Xie, S. P. & Hu, S. Climate impacts of a weakened Atlantic meridional overturning circulation in a warming climate. *Sci. Adv.* **6**, (2020).

15. Jackson, L. C. *et al.* Global and European climate impacts of a slowdown of the AMOC in a high resolution GCM. *Clim. Dyn.* **45**, 3299–3316 (2015).

16. Baker, J. A. *et al.* Continued Atlantic overturning circulation even under climate extremes. *Nature* **638**, 987–994 (2025).

17. Sun, S. & Thompson, A. F. Transient Global Overturning Following the Shutdown of North Atlantic Deep Water Formation. *AGU Adv.* **7**, e2026AV002462 (2026).

18. Cheng, W., Chiang, J. C. H. & Zhang, D. Atlantic Meridional Overturning Circulation (AMOC) in CMIP5 Models: RCP and Historical Simulations. *J. Clim.* **26**, 7187–7197 (2013).

19. Weaver, A. J. *et al.* Stability of the Atlantic meridional overturning circulation: A model intercomparison. *Geophys. Res. Lett.* **39**, 20709 (2012).

20. Bonan, D. B. *et al.* Observational constraints imply limited future Atlantic meridional overturning circulation weakening. *Nat. Geosci.* 1–9 (2025) doi:10.1038/s41561-025-01709-0.

21. Portmann, V., Swingedouw, D., Khattab, O. & Chavent, M. Observational constraints project a ~50% AMOC weakening by the end of this century. *Sci. Adv.* **12**, eadx4298 (2026).

22. Baker, J. A., Watson, A. J. & Vallis, G. K. Meridional overturning circulation in a multibasin model. Part i: Dependence on southern ocean buoyancy forcing. *J. Phys. Oceanogr.* **50**, 1159–1178 (2020).

23. Nadeau, L. P. & Jansen, M. F. Overturning Circulation Pathways in a Two-Basin Ocean Model. *J. Phys. Oceanogr.* **50**, 2105–2122 (2020).

24. Nikurashin, M. & Vallis, G. A Theory of the Interhemispheric Meridional Overturning Circulation and Associated Stratification. *J. Phys. Oceanogr.* **42**, 1652–1667 (2012).

25. Toggweiler, J. R. & Samuels, B. On the Ocean's Large-Scale Circulation near the Limit of No Vertical Mixing. *J. Phys. Oceanogr.* **28**, 1832–1852 (1998).

26. Baker, J. A., Watson, A. J. & Vallis, G. K. Meridional Overturning Circulation in a Multibasin Model. Part II: Sensitivity to Diffusivity and Wind in Warm and Cool Climates. *J. Phys. Oceanogr.* **51**, 1813–1828 (2021).

27. Deng, K. *et al.* Changes of Southern Hemisphere westerlies in the future warming climate. *Atmos. Res.* **270**, 106040 (2022).

28. Lee, S. K. *et al.* Human-induced changes in the global meridional overturning circulation are emerging from the Southern Ocean. *Commun. Earth Environ. 2023 41* **4**, 1–12 (2023).

29. Viebahn, J. & Eden, C. Towards the impact of eddies on the response of the Southern Ocean to climate change. *Ocean Model.* **34**, 150–165 (2010).

30. Forget, G. *et al.* ECCO version 4: An integrated framework for non-linear inverse modeling and global ocean state estimation. *Geosci. Model Dev.* **8**, 3071–3104 (2015).

31. Lumpkin, R. & Speer, K. Global Ocean Meridional Overturning. *J. Phys. Oceanogr.* **37**, 2550–2562 (2007).
32. Lee, S. K. *et al.* Global Meridional Overturning Circulation Inferred From a Data-Constrained Ocean & Sea-Ice Model. *Geophys. Res. Lett.* **46**, 1521–1530 (2019).
33. Reintges, A., Martin, T., Latif, M. & Keenlyside, N. S. Uncertainty in twenty-first century projections of the Atlantic Meridional Overturning Circulation in CMIP3 and CMIP5 models. *Clim. Dyn.* **49**, 1495–1511 (2017).
34. Sun, S., Thompson, A. F. & Eisenman, I. Transient Overturning Compensation between Atlantic and Indo-Pacific Basins. *J. Phys. Oceanogr.* **50**, 2151–2172 (2020).
35. Meinshausen, M. *et al.* The shared socio-economic pathway (SSP) greenhouse gas concentrations and their extensions to 2500. *Geosci. Model Dev.* **13**, 3571–3605 (2020).
36. Hausfather, Z. & Peters, G. P. Emissions – the 'business as usual' story is misleading. *Nature* **577**, 618–620 (2020).
37. Romanou, A. *et al.* Stochastic Bifurcation of the North Atlantic Circulation under a Midrange Future Climate Scenario with the NASA-GISS ModelE. *J. Clim.* **36**, 6141–6161 (2023).
38. Stommel, H. Thermohaline Convection with Two Stable Regimes of Flow. *Tellus* **13**, 224–230 (1961).
39. Volkov, D. L. *et al.* Florida Current transport observations reveal four decades of steady state. *Nat. Commun.* **15**, 7780 (2024).
40. Sun, S., Thompson, A. F., Xie, S. P. & Long, S. M. Indo-Pacific Warming Induced by a Weakening of the Atlantic Meridional Overturning Circulation. *J. Clim.* **35**, 815–832 (2022).
41. Dong, Y. *et al.* Intermodel Spread in the Pattern Effect and Its Contribution to Climate Sensitivity in CMIP5 and CMIP6 Models. *J. Clim.* **33**, 7755–7775 (2020).

42. Bonan, D. B., Thompson, A. F., Newsom, E. R., Sun, S. & Rugenstein, M. Transient and Equilibrium Responses of the Atlantic Overturning Circulation to Warming in Coupled Climate Models: The Role of Temperature and Salinity. *J. Clim.* **35**, 5173–5193 (2022).
43. Pontes, G. M. & Menviel, L. Weakening of the Atlantic Meridional Overturning Circulation driven by subarctic freshening since the mid-twentieth century. *Nat. Geosci.* **17**, 1291–1298 (2024).
44. Bakker, P. *et al.* Fate of the Atlantic Meridional Overturning Circulation: Strong decline under continued warming and Greenland melting. *Geophys. Res. Lett.* **43**, 12,252-12,260 (2016).
45. Boot, A. A. & Dijkstra, H. A. Physics of AMOC multistable regime shifts due to freshwater biases in an EMIC. *Earth Syst. Dyn.* **16**, 1221–1235 (2025).
46. Hankel, C. The effect of CO2 ramping rate on the transient weakening of the Atlantic Meridional Overturning Circulation. *Proc. Natl. Acad. Sci.* **122**, e2411357121 (2025).
47. Stouffer, R. J. & Manabe, S. Response of a Coupled Ocean–Atmosphere Model to Increasing Atmospheric Carbon Dioxide: Sensitivity to the Rate of Increase. *J. Clim.* **12**, 2224–2237 (1999).

Extended Data Figures

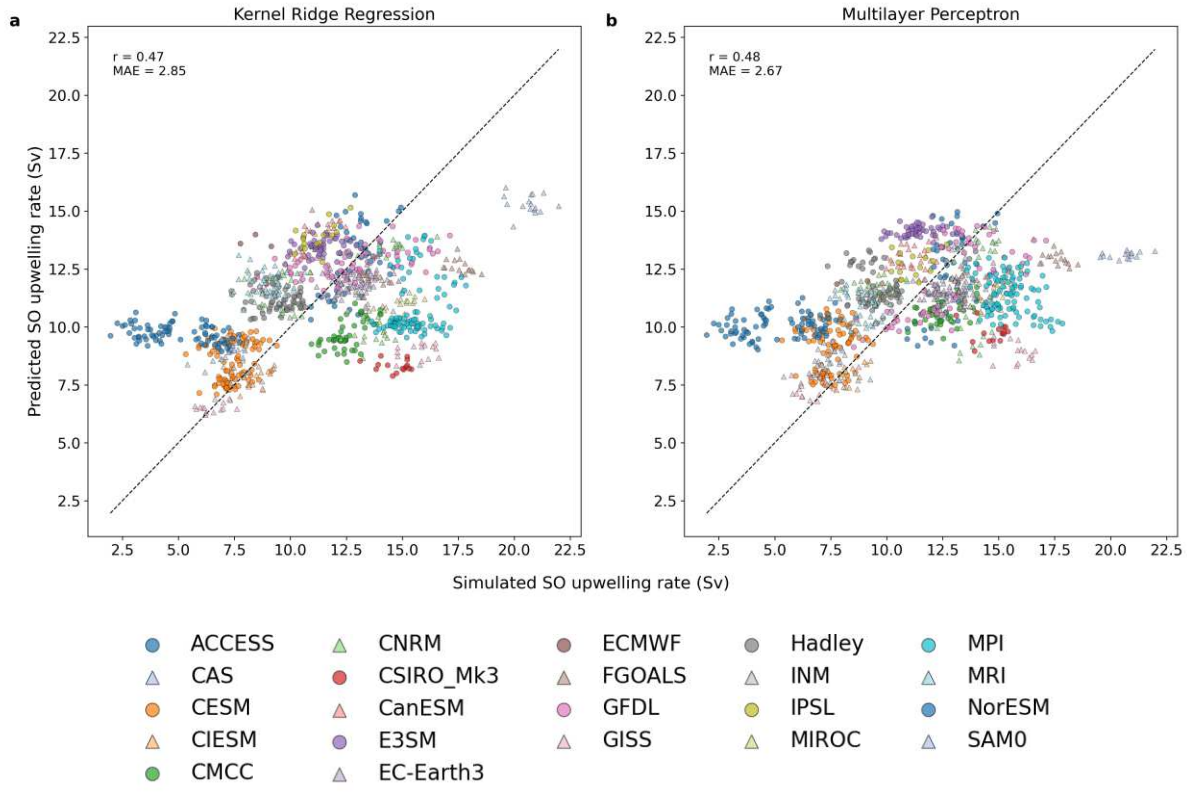

Extended Data Fig. 1: Southern Ocean (SO) upwelling prediction performance of kernel ridge regression and a multilayer perceptron under leave-one-model-family-out cross-validation. a,b, Predicted versus simulated decadal-mean SO upwelling from historical simulations for climate model families using kernel ridge regression **(a)** and a multilayer perceptron **(b)**. All predictions were obtained using leave-one-model-family-out cross-validation. The 1:1 line is shown for reference. Pearson correlation coefficients and mean absolute errors (MAE), averaged across model families, are shown.

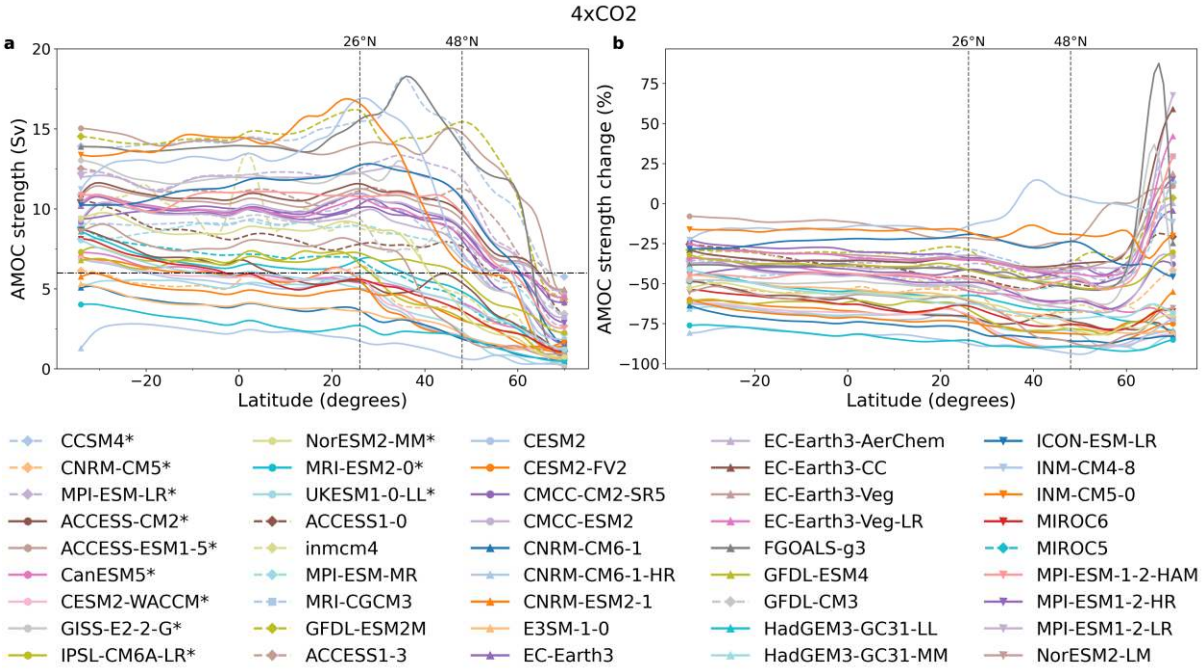

Extended Data Fig. 2: Latitudinal structure of the AMOC under 4xCO2 forcing. (a) AMOC strength after 150 years of 4xCO2 forcing and **(b)** the percentage change in AMOC strength relative to the present day. Dashed (solid) lines denote CMIP5 (CMIP6) models. Vertical dashed lines indicate 26°N and 48°N. The horizontal dashed line in **(a)** marks the 6 Sv AMOC extreme-weakening threshold at 26°N.

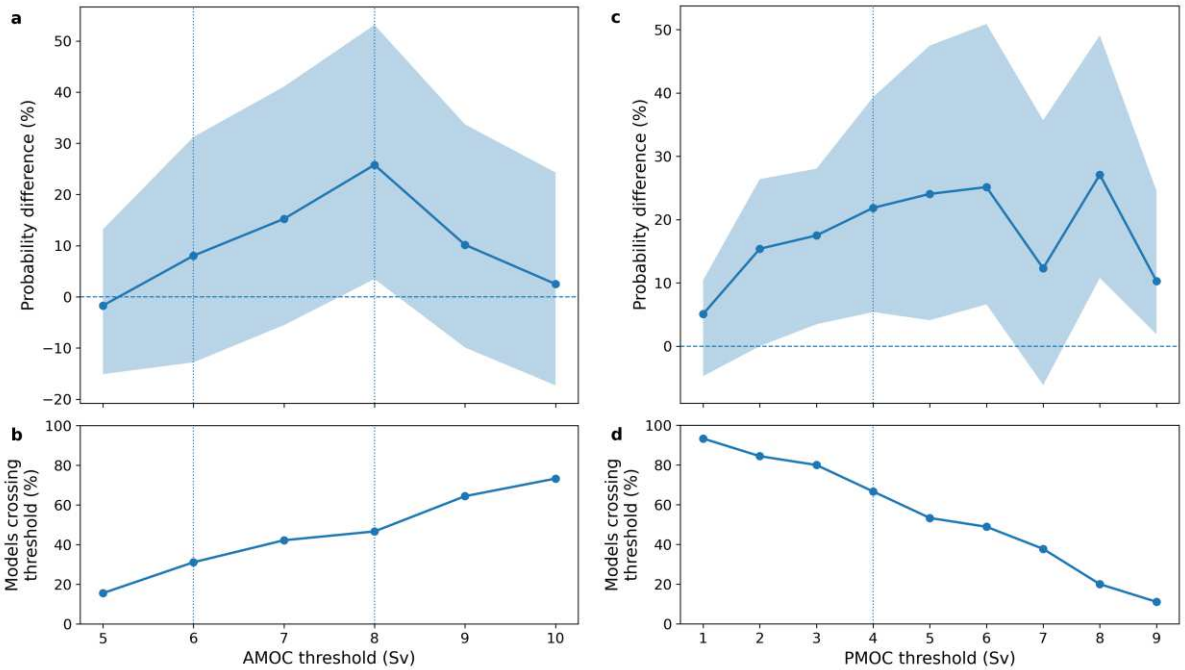

Extended Data Fig. 3: Sensitivity of overturning susceptibility relationships to the state thresholds. Difference in fitted probability from logistic regression across AMOC **(a)** and PMOC **(c)** thresholds within 150 years of 4xCO2 forcing, comparing the 25th and 75th percentiles of control-state SO upwelling (~9 and 13 Sv) **(a)** or control-state Indo-Pacific pathway strength (~2.5 and 7.5 Sv) **(c)**. Contrasts are defined so that positive values indicate greater susceptibility at weaker SO upwelling **(a)** or weaker Indo-Pacific pathway strength **(c)**. Shading shows 95% bootstrap confidence intervals. **(b,d)** Fraction of models weakening below each AMOC threshold **(b)** or exceeding each PMOC threshold **(d)**. The AMOC relationship is most clearly resolved around 8 Sv, where models are more evenly divided between crossing and non-crossing cases.

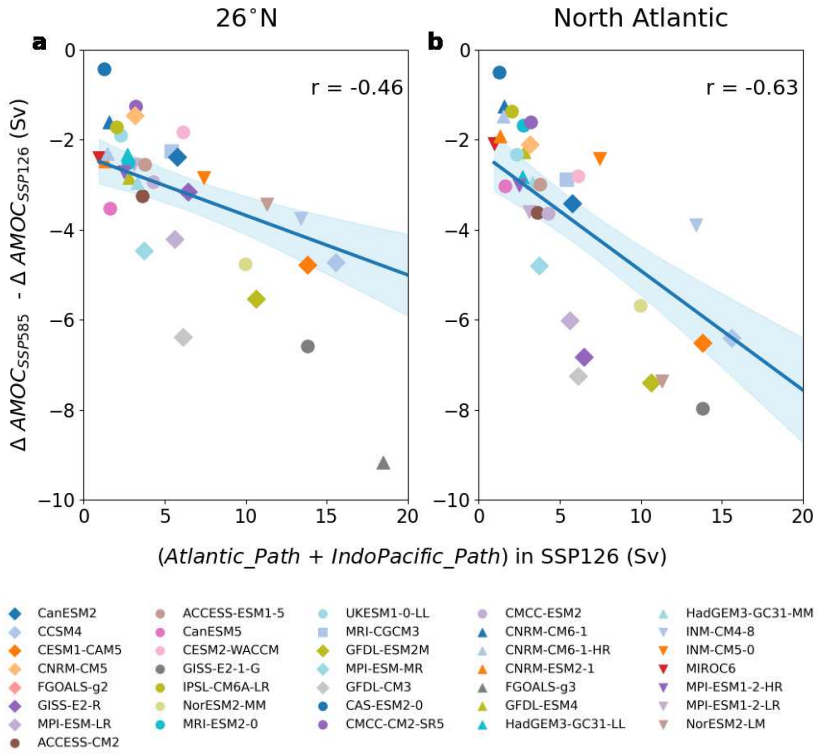

Extended Data Fig. 4: Stronger Atlantic and Indo-Pacific upwelling pathways under SSP126 increase the scenario dependence of AMOC weakening by 2100. Difference in AMOC weakening between SSP585 and SSP126 ($\Delta AMOC_{SSP585} - \Delta AMOC_{SSP126}$) plotted against the sum of the AMOC's Atlantic and Indo-Pacific upwelling pathways in the SSP126 simulation. Differences in AMOC weakening are shown for AMOC strength defined at 26°N **(a)** and the maximum overturning strength in the North Atlantic **(b)**. ΔAMOC is defined relative to the present-day period. Diamonds/squares (circles/triangles) denote CMIP5 (CMIP6) models. Correlations are statistically significant ($p < 0.05$).

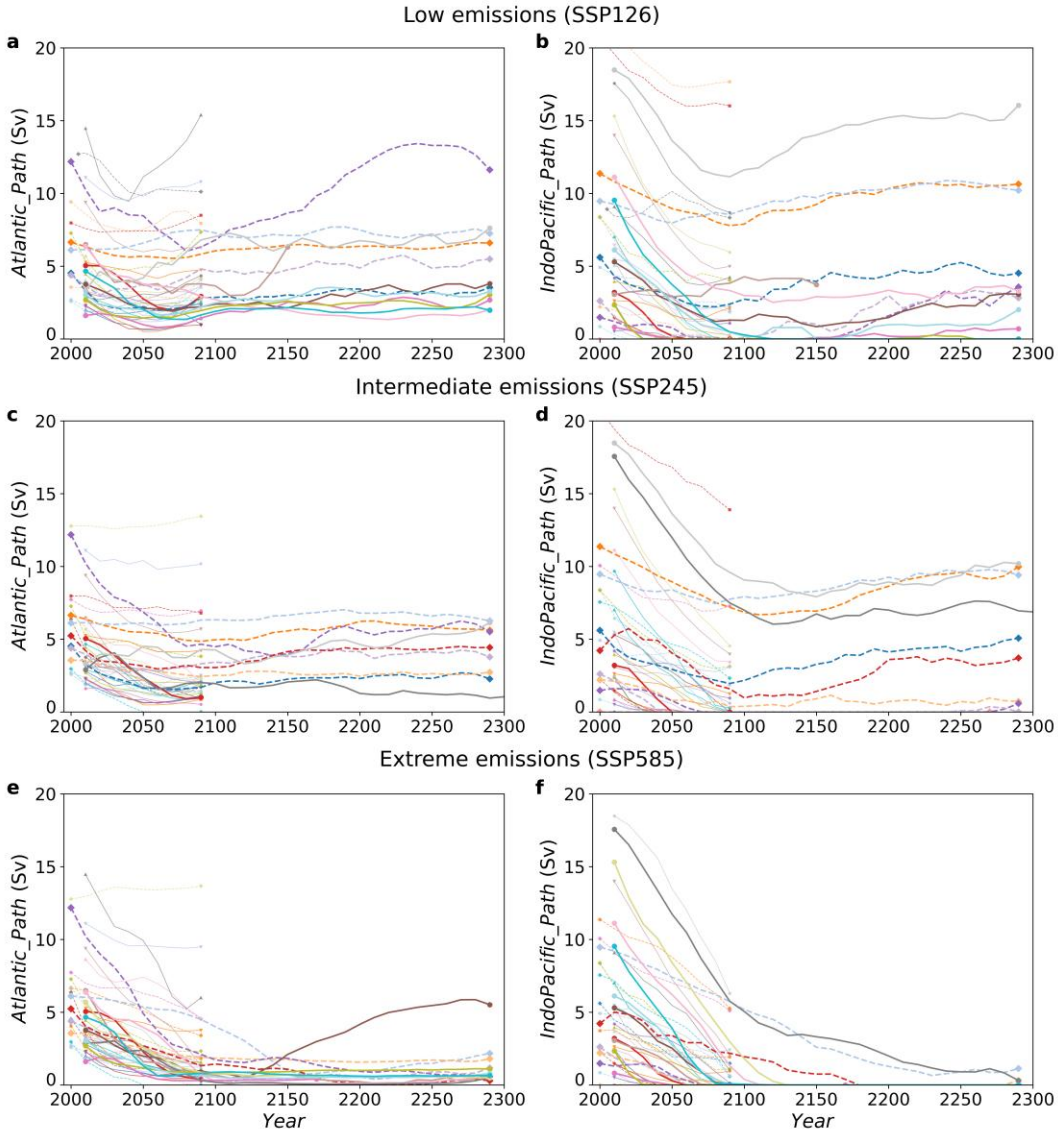

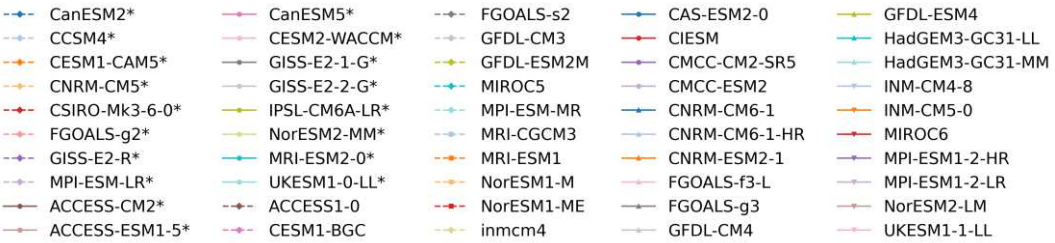

Extended Data Fig. 5: AMOC's Atlantic and Indo-Pacific upwelling pathways weaken before 2100 and diverge thereafter across emissions scenarios. a–f Atlantic **(a,c,e)** and Indo-Pacific **(b,d,f)** upwelling pathways of the AMOC. Rows show low- (SSP1-2.6/RCP2.6) **(a,b)**, intermediate- (SSP2-4.5/RCP4.5) **(c,d)**, and extreme-emissions (SSP5-8.5/RCP8.5) **(e,f)** scenarios. Dashed (solid) coloured lines denote CMIP5 (CMIP6) models, with faint (bold) lines indicating simulations ending in 2100 (2300). Models with simulations extended beyond 2100 are labelled with an asterisk. Time series are shown as decadal means and smoothed using a 3-point centred running mean for visual clarity.

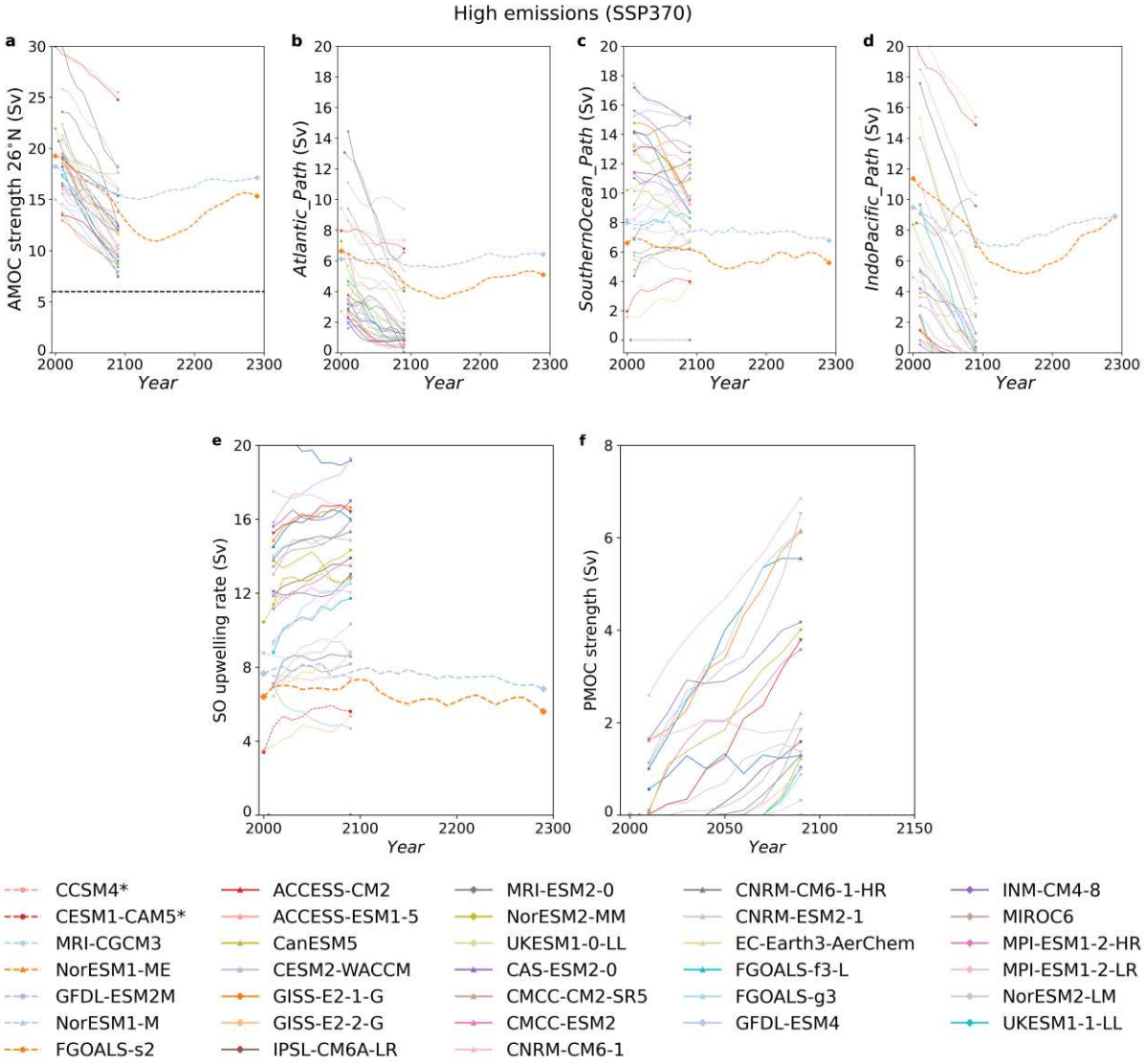

Extended Data Fig. 6: **Evolution of AMOC strength, its upwelling pathways, Southern Ocean upwelling, and PMOC strength under high-emissions (SSP3-7.0/RCP6.0) scenarios. a–d** AMOC strength at 26°N, and the AMOC's Atlantic, Southern Ocean, and Indo-Pacific upwelling pathways, respectively. **(e**,**f)** Southern Ocean upper cell strength at 34.5°S and Pacific meridional overturning circulation (PMOC) strength at 34.5°S, respectively. Dashed (solid) lines denote CMIP5 (CMIP6) models. Time series are shown as decadal means and smoothed using a 3-point centred running mean for visual clarity. The upwelling pathways shown in **(b–d)** sum to approximately the AMOC strength shown in **(a)**.

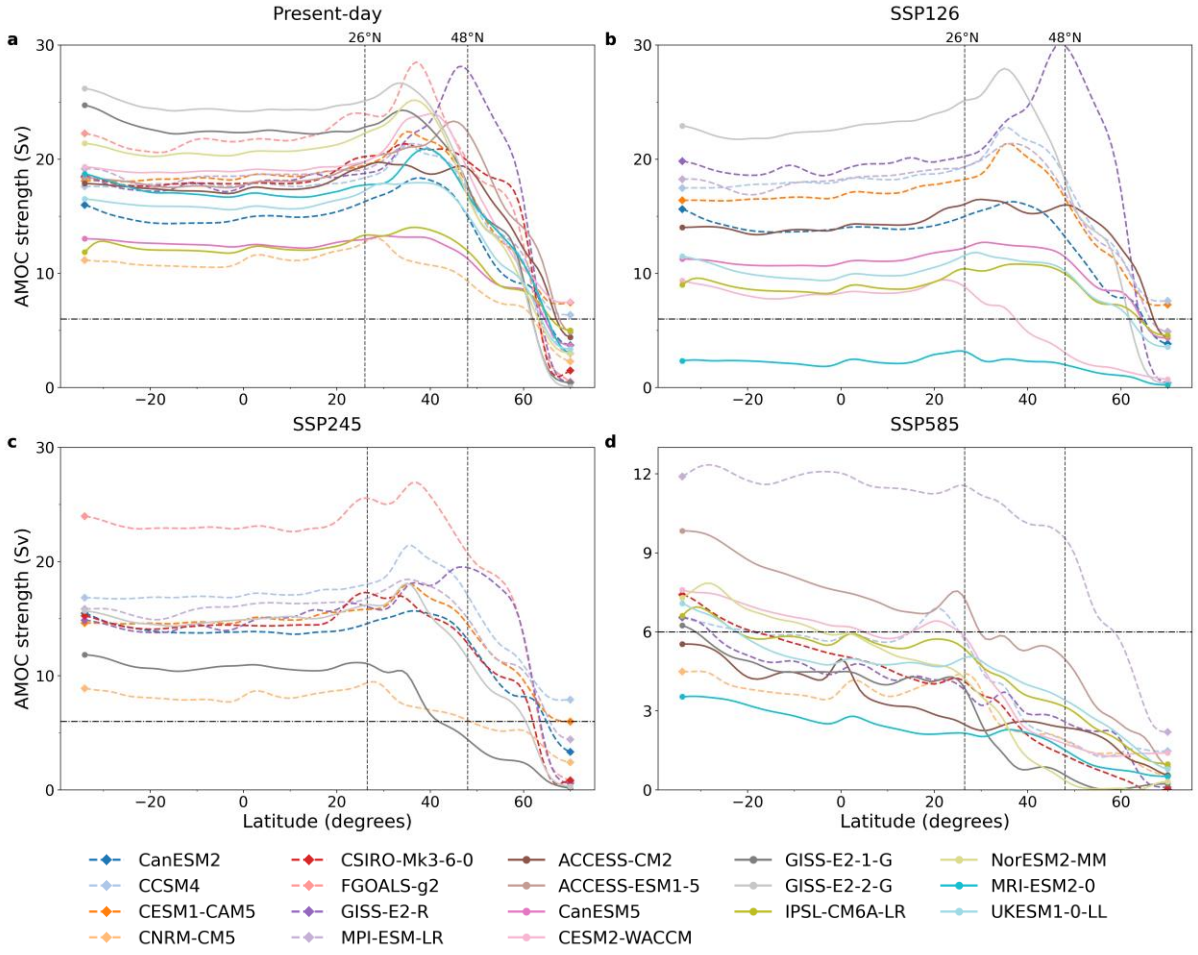

563

564

565 **Extended Data Fig. 7: Latitudinal structure of the AMOC under present-day conditions and future**
566 **climate forcing scenarios.** Panels show AMOC strength as a function of latitude for the present day **(a)** and in
567 2300 under SSP126 **(b)**, SSP245 **(c)**, and SSP585 **(d)**. Dashed (solid) lines denote CMIP5 (CMIP6) models.
568 Vertical dashed lines indicate 26°N and 48°N. The horizontal dashed line marks the 6 Sv AMOC extreme-
569 weakening threshold at 26°N.

570

571

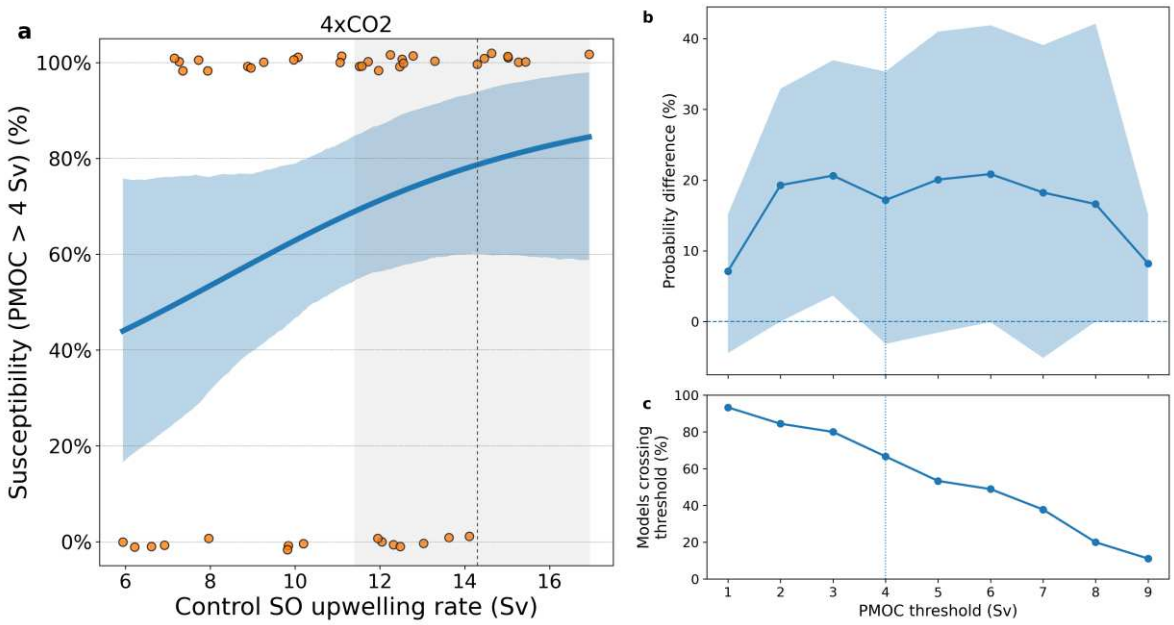

Extended Data Fig. 8: Stronger Southern Ocean upwelling is associated with greater susceptibility to PMOC development. **(a)** Logistic regression estimate of the probability that the PMOC exceeds 4 Sv within 150 years of abrupt 4xCO2 forcing as a function of control-state SO upwelling. Points show individual model outcomes (100% if the PMOC exceeds 4 Sv and 0% otherwise; vertically offset for clarity), the blue line shows the fitted probability and shading indicates the 95% bootstrap confidence interval. **(b)** Difference in fitted probabilities between the 75th and 25th percentiles of control-state SO upwelling (~13 and 9 Sv) across PMOC thresholds. Positive values indicate greater PMOC susceptibility in models with stronger SO upwelling. Shading shows 95% bootstrap confidence intervals.

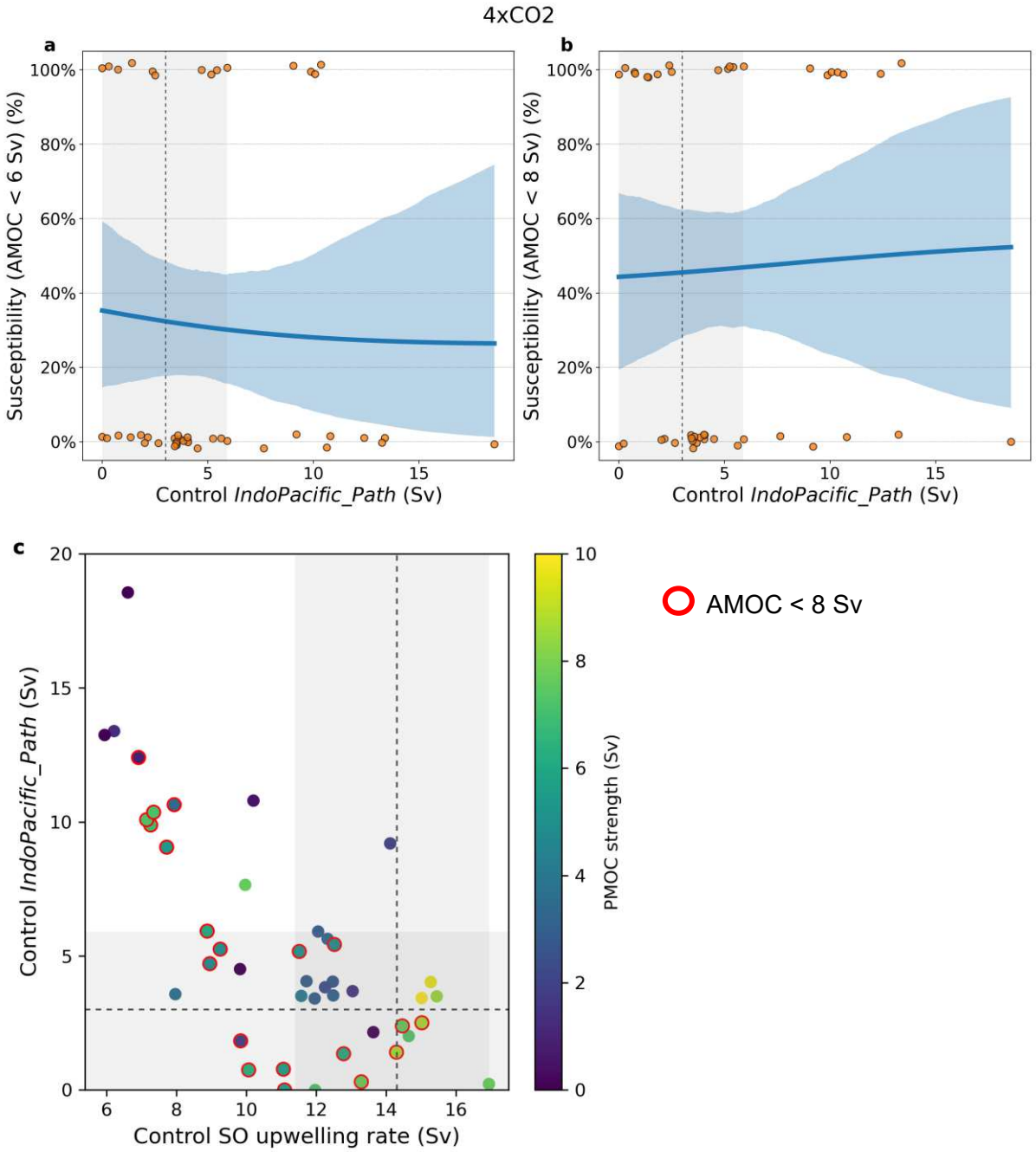

Extended Data Fig. 9: Indo-Pacific pathway strength is not a robust predictor of susceptibility to very weak AMOC states. a,b, Logistic regression estimates of the probability that the AMOC weakens below 6 Sv **(a)** and 8 Sv **(b)** at 26°N within 150 years of 4xCO2 forcing, as a function of control Indo-Pacific pathway strength. Points show individual model outcomes (100% if the AMOC weakens below the threshold and 0% otherwise; vertically offset for clarity), the blue line shows the fitted probability and shading indicates the 95% bootstrap confidence interval. **(c)** Joint distribution of control SO upwelling and Indo-Pacific pathway strength across models. Colours indicate PMOC strength over the final decade of the 150-year 4xCO2 simulations; red outlines denote models with decadal-mean AMOC strength below 8 Sv at 26°N over the same period.

Experiment	Model Intercomparison Project	Number of models (decadal-mean samples)
Historical[48,49]	CMIP5/6	60 (940)
SSP1-2.6[48]	CMIP6	23 (173)
SSP2-4.5[48]	CMIP6	21 (168)
SSP3-7.0[48]	CMIP6	16 (97)
SSP5-8.5[48]	CMIP6	25 (200)
RCP2.6[49]	CMIP5	9 (81)
RCP4.5[49]	CMIP5	8 (72)
RCP6.0[49]	CMIP5	5 (45)
RCP8.5[49]	CMIP5	10 (90)
Abrupt-4xCO2[48,49]	CMIP5/6	29 (427)
1%CO2[48,49]	CMIP5/6	35 (488)
Hist-1950[50]	HighResMIP	2 (6)
Highres-future[50]	HighResMIP	1 (3)
faf-stress[51]	FAFMIP	8 (56)
SOFIA[52]	SOFIA	3 (48)
Total	–	64 (2741)

Extended Data Table 1: CMIP5 and CMIP6 experiments used to train the regression models. Lists of the CMIP5 and CMIP6 experiments included in the training dataset for the kernel ridge regression and multilayer perceptron models, together with the corresponding number of climate models and decadal-mean samples.

Model Family	Models
ACCESS	ACCESS-CM2, ACCESS-ESM1-5, ACCESS1-0
CanESM	CanESM2, CanESM5
CAS	CAS-ESM2-0
MPI	MPI-ESM-LR, MPI-ESM-MR, MPI-ESM-P, MPI-ESM-1-2-HAM, MPI-ESM1-2-LR', MPI-ESM1-2-HR
CESM	CESM1-CAM5, CESM1-BGC, CESM2 CESM2-FV2, CESM2-WACCM, CCSM4
CIESM	CIESM
CMCC	CMCC-CM2-HR4, CMCC-CM2-SR5, CMCC-ESM2
CNRM	CNRM-CM5, CNRM-CM5-2, CNRM-CM6-1, CNRM-CM6-1-HR, CNRM-ESM2-1
CSIRO_Mk3	CSIRO-Mk3-6-0
E3SM	E3SM-1-0, E3SM-1-1, E3SM-1-1-ECA
EC-Earth3	EC-Earth3, EC-Earth3-AerChem, EC-Earth3-CC, EC-Earth3-Veg, EC-Earth3-Veg-LR
ECMWF	ECMWF-IFS-HR
FGOALS	FGOALS-f3-L, FGOALS-g3
GFDL	GFDL-CM3, GFDL-CM4, GFDL-ESM2M, GFDL-ESM4
GISS	GISS-E2-1-G, GISS-E2-2-G, GISS-E2-R
Hadley	HadGEM3-GC31-LL, HadGEM3-GC31-MM, HadGEM3-GC31-HH, UKESM1-0-LL, UKESM1-1-LL
INM	INM-CM4-8, INM-CM5-0
IPSL	IPSL-CM6A-LR
MIROC	MIROC6
MRI	MRI-CGCM3, MRI-ESM1, MRI-ESM2-0
NorESM	NorCPM1, NorESM1-M, NorESM1-ME, NorESM2-LM, NorESM2-MM
SAM0	SAM0-UNICON

Extended Data Table 2: CMIP5 and CMIP6 model families used for leave-one-model-family-out cross-validation. List of the CMIP5 and CMIP6 model families and the associated climate models used to define the leave-one-model-family-out cross-validation folds.

Methods

Climate models and experiments

We use output from 64 CMIP5 and CMIP6 climate models across 15 experiments (Extended Data Table 1) to train the regression models and analyse changes in the AMOC and its upwelling pathways. We analyse four CMIP5 Representative Concentration Pathway (RCP) experiments[49] and four CMIP6 Shared Socioeconomic Pathway (SSP) experiments [48], including all available simulations extending beyond 2100. These span low- to extreme-emissions scenarios, with radiative forcing in 2100 ranging from 2.6 to 8.5 W m^{-2}[53,54]. Related CMIP5 and CMIP6 scenarios are grouped (e.g. RCP2.6 and SSP1-2.6 as SSP126; RCP6.0 and SSP3-7.0 as SSP370).

We also analyse the abrupt-4xCO2 experiment (4xCO2)[48], in which atmospheric CO_2 concentrations are instantaneously quadrupled from pre-industrial levels and maintained for 150 years. We analyse one ensemble member per model. Where multiple extended simulations of a model show substantially different AMOC responses (e.g., GISS-E2-1-G), we retain the member with greatest weakening because these extended simulations are used to diagnose circulation pathways associated with extreme responses rather than to estimate their probability.

Observational data

We use EN4 objective analysis data (with the XBT[55] and MBT[56] corrections) and World Ocean Atlas (WOA) 2023[57,58], to calculate the observational inputs to the regression model. Both are processed identically to the climate model fields. Because they draw on largely overlapping in-situ observations, they are not independent constraints, although they differ in quality control and analysis methodology. We use observations from 2005–2024.

For comparison with our SO upwelling (i.e., SO upper cell strength at 34.5°S) estimate, we use three observation-based products: ECCOv4[30], an inverse-model estimate[31], and a robust diagnostic simulation estimate[32]. We also use estimates of South Atlantic overturning strength at 34.5°S from these and other observation-based products[59,60] and from the SAMBA observing array[61] to estimate the AMOC upwelling pathways.

Variables

We analyse the monthly-mean overturning mass streamfunction in depth space, including Eulerian-mean and parameterised eddy components[62]. For emergent constraint analyses, fields are averaged over the final 10 years of the historical simulation (the present-day period) and the 20-year period centred on 2090 in the RCP and SSP simulations.

AMOC strength is defined as the maximum Atlantic overturning streamfunction at 26°N below 500 m depth, where present-day northward heat transport peaks[63]. This excludes the localised subtropical gyre circulation while retaining waters transported northward that subsequently sink below 500 m. Extreme AMOC weakening is defined as decadal-mean AMOC strength below 6 Sv at 26°N and below 500 m. We also calculate AMOC strength below 500 m across the Atlantic to assess its spatial structure.

PMOC strength is defined as the maximum Indo-Pacific overturning streamfunction at 34.5°S between 500 and 4000 m depth, excluding wind-driven gyres and unrelated deep overturning circulations. The Southern Ocean is defined as latitudes south of 34.5°S.

Monthly-mean time series are averaged into decadal means and smoothed with a 3-point centred running mean for visualisation. The first and last decadal means are unsmoothed. All analyses use unsmoothed decadal means.

AMOC upwelling pathways

Upwelling pathway definitions

We diagnose AMOC upwelling pathways following ref.[10,16]. These quantify the volume transports returning deep AMOC waters from the southward to the shallower northward branch. Three non-negative pathways partition the AMOC return flow and sum to the maximum North Atlantic overturning strength: Atlantic upwelling (Atlantic_Path; Eq. S1), Southern Ocean upwelling (SouthernOcean_Path; Eq. S2-S3) and Indo-Pacific residual upwelling (IndoPacific_Path; Eq. S4).

Since the pathways are diagnosed from the maximum North Atlantic overturning rather than the AMOC strength at 26°N, their summed transport can exceed the AMOC at 26°N, particularly when overturning is stronger elsewhere in the North Atlantic. They are derived from the zonally-integrated overturning streamfunction in the Atlantic and Indo-Pacific and the globally-integrated overturning streamfunction south of 34.5°S. Transports are expressed in Sverdrups (1 Sv = 10^6 m^3 s^{-1}).

Atlantic_Path returns AMOC deep waters within the Atlantic. SouthernOcean_Path represents upwelling of North Atlantic-origin waters by the SO upper cell, including waters that first upwell in the Indo-Pacific. IndoPacific_Path is the residual Indo-Pacific upwelling of AMOC deep waters that do not subsequently upwell in the SO. Changes in AMOC strength are balanced by changes in these return pathways through fast, non-advective wave-driven adjustment[34], enforcing an upwelling–downwelling constraint on decadal and longer timescales.

The pathways are similar in density and depth space[10,16,22]. We use depth space because overturning streamfunctions in density space are available for only a few models.

South Atlantic and Indo-Pacific overturning cells

Some models have weak overturning related sinking in the South Atlantic at 34.5°S that is disconnected from the North Atlantic. Following ref.[16], this component (South_Atlantic_local; Eq. S3) is accounted for when diagnosing Atlantic_Path and SouthernOcean_Path. In historical simulations, South_Atlantic_local and PMOC are generally weak or absent, allowing present-day SO upper cell strength at 34.5°S to approximate SouthernOcean_Path.

A PMOC balances part of the SO upper cell upwelling and reduces the upwelling available to return AMOC deep waters. SouthernOcean_Path is therefore capped at the southward AMOC transport into the SO ($AMOC_{min}$; Eq. S2) when diagnosed SO upwelling exceeds this transport. During initial PMOC development, the PMOC contribution is removed explicitly. This maintains volume conservation; the approach is validated in ref.[16].

AMOC upwelling pathway equations

The AMOC upwelling pathways are calculated as:

$$\text{Atlantic_Path} = AMOC_{max} - AMOC_{min} \quad \text{(S1)}$$

$$\text{SouthernOcean_Path} = \min\left(\psi_{max}\big|_{34.5°S} - \text{South_Atlantic_local} - \text{PMOC}\big|_{z_AMOC_34.5°S}, AMOC_{min}\right) \quad \text{(S2)}$$

where,

$$\text{South_Atlantic_local} = \text{AMOC_34S} - AMOC_{min} \quad \text{(S3)}$$

$$\text{IndoPacific_Path} = AMOC_{max} - \text{Atlantic_Path} - \text{SouthernOcean_Path} \quad \text{(S4)}$$

Here, $AMOC_{max}$ is the maximum AMOC strength north of the equator. $AMOC_{min}$ (≥ 0 Sv) is the minimum value of the maximum AMOC strength between 34.5°S and the equator, and AMOC_34S is the AMOC strength at 34.5°S. $PMOC\,|_{z_AMOC_34.5°S}$ is the PMOC strength (≥ 0 Sv) at 34.5°S evaluated at the depth of the AMOC maximum at 34.5°S. $\psi_{max}\,|_{34.5°S}$ is the maximum globally-integrated SO upper cell strength at 34.5°S, defining the SO upwelling rate.

Observation-based Indo-Pacific pathway estimate

We estimate the present-day Indo-Pacific residual upwelling pathway by combining our regression-based SO upwelling estimate with observation-based South Atlantic overturning at 34.5°S. In the present-day climate, the PMOC is generally weak or absent, and the South Atlantic local overturning component ("South_Atlantic_local") is explicitly accounted for in the pathway calculation (Eqs. S2–S3). Under these conditions, $AMOC_{min}$ cancels from the residual (Eq. S4), such that the Indo-Pacific pathway is approximately the difference between AMOC strength at 34.5°S and SO upper cell strength at the same latitude.

We therefore use the SAMBA estimate of South Atlantic upper cell overturning at 34.5°S (17.3 ± 5.0 Sv; mean ± estimated systematic bias)[61] rather than AMOC strength at 26.5°N. Combining the SAMBA mean with our SO upwelling estimate of 14.3 Sv gives a present-day Indo-Pacific pathway of 3.0 Sv. Holding the SAMBA mean fixed, the 10–90% uncertainty in SO upwelling gives a pathway range of 0–5.9 Sv. Negative residuals are set to zero because pathway strengths are non-negative by definition.

The 0–5.9 Sv range therefore reflects SO upwelling uncertainty conditional on the SAMBA mean. Because the ±5.0 Sv SAMBA bias is not a probabilistic confidence interval, we treat it separately rather than combine it with SO upwelling uncertainty. Independent estimates of South Atlantic overturning provide context for this additional uncertainty. ndependent South Atlantic overturning estimates provide context: observation-based central estimates span values both below and above the SAMBA mean, with the upper end around 20 Sv[10,59,64]. These estimates differ in period, methodology and overturning definition and carry their own uncertainties, so their spread is not a formal uncertainty distribution. Nevertheless, they do not indicate a systematic shift towards substantially stronger South Atlantic overturning than SAMBA, while several imply weaker overturning and hence a weaker Indo-Pacific pathway.

As an independent check, paired estimates of SO upper cell strength and South Atlantic overturning from ECCOv4[30], an inverse-model[31] and a robust diagnostic simulation[32] imply

Indo-Pacific pathway strengths of 0–6.5 Sv, consistent with a relatively weak present-day pathway.

Present-day Indo-Pacific pathway and future PMOC development

We test whether present-day Indo-Pacific pathway strength predicts future PMOC development across emissions scenarios. Present-day pathway strength is averaged over the final 10 years of the historical simulations, and PMOC strength over the 20 years centred on 2090. Corresponding CMIP5 RCP and CMIP6 SSP scenarios are combined because of similar forcing by 2100 and to increase sample size. For each scenario group, we regress late-century PMOC strength against present-day Indo-Pacific pathway strength (Fig. 5). The observation-based Indo-Pacific pathway estimate and its 10–90% uncertainty range are shown relative to these model relationships.

Logistic regression of extreme weakening susceptibility

We use binomial logistic regression to estimate the probability that the AMOC falls below a specified threshold within 150 years of abrupt-4xCO2 forcing as a function of control-state SO upwelling. For each model and threshold, the response is one if decadal-mean AMOC at 26°N falls below the threshold at any time and zero otherwise. We analyse the 6 Sv extreme-weakening threshold and an additional 8 Sv threshold, and repeat the analysis at 48°N.

Threshold sensitivity is assessed from 5–10 Sv in 1 Sv increments (Extended Data Fig. 3a,c). At each threshold, we calculate the difference between fitted probabilities at the 25th and 75th percentiles of control-state SO upwelling (~9 and 13 Sv), held fixed across thresholds. Positive values indicate greater susceptibility with weaker SO upwelling. We also calculate the fraction of models crossing each threshold.

Uncertainty in fitted probabilities and probability contrasts is estimated from 2000 bootstrap resamples of models with replacement, with 95% confidence intervals derived from the bootstrap distribution.

To test sensitivity to dependence among related models, we repeat the analysis across 17 model families representing shared model development centres. For each family, we use family-mean SO upwelling as the predictor and the fraction of family members crossing each threshold as the response. Family-level fits show declines in susceptibility with increasing SO upwelling similar to those in the individual model analysis, but with wider confidence intervals due to the smaller effective sample size. We also repeat the analysis separately for

CMIP5 and CMIP6. The negative relationship between SO upwelling and susceptibility is more pronounced in CMIP6, whereas it is less well constrained in CMIP5, where fewer models reach very weak AMOC states.

We similarly use logistic regression to estimate the probability that PMOC strength exceeds 4 Sv within 150 years of 4xCO2 forcing as a function of control-state Indo-Pacific pathway strength. Threshold sensitivity is assessed across a range of PMOC strengths, with probability contrasts evaluated between the 25th and 75th percentiles of pathway strength (Extended Data Fig. 3c,d). Uncertainty is estimated using the same bootstrap procedure.

Significance tests

Linear and logistic regression coefficients are assessed using two-tailed Student's t-test and Wald tests, respectively, with $P<0.05$ considered significant. For linear regressions, 95% confidence intervals use standard Student's t-based formulas.

Non-linear regression model

We estimate SO upwelling (i.e., SO upper overturning circulation strength at 34.5°S) from large-scale ocean density structure and scalar predictors. The models are designed to generalise to unseen climate models rather than reproduce individual model behaviour as our objective is to infer present-day SO upwelling from observations. Our primary estimate uses kernel ridge regression with a radial basis function (RBF) kernel, implemented in scikit-learn[65], with regularisation parameter, $\alpha = 0.1$, and kernel width, $\gamma = 0.0005$. Kernel ridge regression is used as the primary model because it achieves predictive skill comparable to more complex machine-learning approaches while remaining simpler. As a robustness check, we use a multilayer perceptron (MLP) with two fully connected hidden layers of 64 and 32 units and ReLU activation functions.

Inputs and preprocessing

The primary input is a zonal section of potential density at 34.5°S, interpolated onto a common longitude–depth grid (360 longitude points; 29 levels between 15 and 1615 m depth) matching EN4. Potential density is calculated from conservative temperature and absolute salinity using the TEOS-10 equation of state. Inputs and targets are averaged into decadal means to reduce high-frequency variability and to focus on the timescales relevant to long-term overturning changes. Each decadal-mean density field constitutes one training sample.

Additional scalar predictors are near-surface (15 m) zonal-mean potential temperature at 34.5°S and experiment type encoded as one-hot categorical variables. SO wind stress metrics were also tested but did not improve cross-validated skill. The target variable is SO upwelling, diagnosed from the global upper cell overturning at 34.5°S.

Density fields are standardised per sample to zero mean and unit variance, flattened after removing land points, and projected onto principal components derived from the training data. Scalar predictors and the target variable are scaled to the range 0–1 using Min–Max scaling. All standardisation, principal-component and scaling transformations are fitted using training data only within each cross-validation fold. We retain the leading 120 principal components, selected by cross-validation. Predictions are transformed back into physical units of Sverdrups.

Model training and validation

The regression models are trained on 2900 decadal-mean samples from 64 climate models across 15 CMIP5 and CMIP6 experiments (Extended Data Table 1), spanning a wide range of historical and forced overturning states.

Hyperparameters are selected using five-fold cross-validation, with final performance evaluated using leave-one-model-family-out cross-validation. All samples from each model family, defined by shared model-development centres (Extended Data Table 2), are withheld together during testing. This is more stringent than model-wise cross-validation because related models cannot appear in both training and test sets, providing a more conservative estimate of predictive uncertainty and better testing generalisation to structurally distinct model families.

Performance is stable across a broad range of hyperparameters, including principal component counts above 20, $\gamma < 0.01$, and $\alpha > 5 \times 10^{-4}$, and declines only for more extreme values. Among models with similar mean absolute error (MAE), stronger regularisation is preferred to reduce overfitting.

For the MLP, training is repeated across random initialisations and predictions are averaged across ten independently trained models to reduce stochastic variability. Early stopping is used to reduce overfitting. Model skill is assessed primarily using MAE.

Observational prediction

The final kernel ridge regression is trained on all climate model data using the selected hyperparameters. EN4 and WOA from 2005–2024 are processed using the same transformations as the climate model data. EN4 provides the final estimate of 14.3 Sv, while WOA gives a value only 0.1 Sv weaker. The independently trained MLP gives 13.1 Sv, providing a robustness check on the regression method.

The resulting SO upwelling estimate is used to constrain susceptibility to very weak AMOC states and, together with observed AMOC strength, to estimate the present-day Indo-Pacific pathway.

Uncertainty estimation

Prediction uncertainty is estimated from leave-one-model-family-out cross-validation. For each withheld model family, we calculate the mean prediction error (true minus predicted SO upwelling) and aggregate errors across validation folds. The 10th and 90th percentiles of this distribution define the prediction interval around the observational estimate. For kernel ridge regression this gives 11.4–18.8 Sv (MAE = 2.85 Sv; $R^2 = 0.22$ across historical simulations; Extended Data Fig. 1a), primarily representing prediction uncertainty associated with structural differences among climate models.

The uncertainty interval does not explicitly propagate uncertainty in the observational input fields. Decadal averaging reduces random observational errors, while per-sample standardisation reduces sensitivity to spatially uniform density biases. EN4 and WOA yield similar predictions, indicating limited sensitivity to the observational density product. Explicit propagation of density field uncertainties through the non-linear regression is beyond the scope of this study.

Uncertainty is estimated from historical samples because the 2005-2024 observations are most comparable to the historical simulations; similar predictive skill is obtained when all experiments are included. For the MLP, leave-one-model-family-out validation gives a 10–90% range of 10.4–17.2 Sv ($R^2 = 0.22$; Extended Data Fig. 1b), compared with 11.1–16.9 Sv ($R^2 = 0.61$) under less stringent leave-one-model-out validation.

Data availability

The CMIP5 and CMIP6 data used in this study are available at https://esgf-index1.ceda.ac.uk/search/ and https://esgf-node.ornl.gov/search.

Code availability

The code used to calculate the AMOC's upwelling pathways is available at https://doi.org/10.5281/zenodo.11116004[66].

Methods Refereneces

48. Eyring, V. *et al.* Overview of the Coupled Model Intercomparison Project Phase 6 (CMIP6) experimental design and organization. *Geosci. Model Dev.* **9**, 1937–1958 (2016).
49. Taylor, K. E., Stouffer, R. J. & Meehl, G. A. An Overview of CMIP5 and the Experiment Design. *Bull. Am. Meteorol. Soc.* **93**, 485–498 (2012).
50. Haarsma, R. J. *et al.* High Resolution Model Intercomparison Project (HighResMIP v1.0) for CMIP6. *Geosci. Model Dev.* **9**, 4185–4208 (2016).
51. Gregory, J. M. *et al.* The Flux-Anomaly-Forced Model Intercomparison Project (FAFMIP) contribution to CMIP6: investigation of sea-level and ocean climate change in response to CO_2 forcing. *Geosci. Model Dev.* **9**, 3993–4017 (2016).
52. Swart, N. C. *et al.* The Southern Ocean Freshwater Input from Antarctica (SOFIA) Initiative: scientific objectives and experimental design. *Geosci. Model Dev.* **16**, 7289–7309 (2023).
53. O'Neill, B. C. *et al.* The Scenario Model Intercomparison Project (ScenarioMIP) for CMIP6. *Geosci Model Dev* **9**, 3461–3482 (2016).
54. van Vuuren, D. P. *et al.* The representative concentration pathways: an overview. *Clim. Change* **109**, 5 (2011).
55. Cowley, R., Wijffels, S., Cheng, L., Boyer, T. & Kizu, S. Biases in Expendable Bathythermograph Data: A New View Based on Historical Side-by-Side Comparisons. *J. Atmos. Ocean. Technol.* **30**, 1195–1225 (2013).

56. Levitus, S. *et al.* Global ocean heat content 1955–2008 in light of recently revealed instrumentation problems. *Geophys. Res. Lett.* **36**, (2009).
57. Locarnini, R. A. *et al.* World Ocean Atlas 2023, Volume 1: Temperature. https://repository.library.noaa.gov (2024) doi:10.25923/54bh-1613.
58. Reagan, J. R. *et al.* World Ocean Atlas 2023, Volume 2: Salinity. https://repository.library.noaa.gov (2024) doi:10.25923/70qt-9574.
59. Baker, J. A. *et al.* South Atlantic overturning and heat transport variations in ocean reanalyses and observation-based estimates. *State Planet* **1-osr7**, 1–15 (2023).
60. Dong, S. *et al.* Synergy of In Situ and Satellite Ocean Observations in Determining Meridional Heat Transport in the Atlantic Ocean. *J. Geophys. Res. Oceans* **126**, e2020JC017073 (2021).
61. Kersalé, M. *et al.* Highly variable upper and abyssal overturning cells in the South Atlantic. *Sci. Adv.* **6**, (2020).
62. Griffies, S. M. *et al.* OMIP contribution to CMIP6: experimental and diagnostic protocol for the physical component of the Ocean Model Intercomparison Project. *Geosci Model Dev* **9**, 3231–3296 (2016).
63. Trenberth, K. E., Zhang, Y., Fasullo, J. T. & Cheng, L. Observation-Based Estimates of Global and Basin Ocean Meridional Heat Transport Time Series. *J. Clim.* **32**, 4567–4583 (2019).
64. Manta, G. *et al.* The South Atlantic Meridional Overturning Circulation and Mesoscale Eddies in the First GO-SHIP Section at 34.5°S. *J. Geophys. Res. Oceans* **126**, e2020JC016962 (2021).
65. Pedregosa, F. *et al.* Scikit-learn: Machine Learning in Python. *J. Mach. Learn. Res.* **12**, 2825–2830 (2011).
66. Jonathan, B. *et al.* A Tool for Calculating AMOC Upwelling Pathways. https://doi.org/10.5281/zenodo.11116004 (2025) doi:10.5281/zenodo.11116004.

Acknowledgements

This is ClimTip contribution X; the ClimTip project has received funding from the European Union's Horizon Europe research and innovation programme under grant agreement No. 101137601. J.A.B, L.C.J, M.J.B and R.A.W were supported by the Met Office Hadley Centre Climate Programme funded by DSIT. We acknowledge the World Climate Research Programme, which, through its Working Group on Coupled Modelling, coordinated and promoted CMIP6. We thank the climate modelling groups for producing and making available their model output, the Earth System Grid Federation (ESGF) for archiving the data and providing access, and the multiple funding agencies who support CMIP6 and ESGF. For the purpose of open access, the author has applied a Creative Commons Attribution (CC BY) licence to any Author Accepted Manuscript version arising from this submission.

Author Contributions

J.A.B conceived the study, performed the analysis, interpreted the results, generated the figures, and wrote the original draft manuscript. J.A.B, M.J.B, L.C.J, G.K.V, A.J.W and R.A.W discussed the results and reviewed and edited the manuscript.

Competing interests

The authors declare no competing interests.

Additional information

Correspondence and requests for materials should be addressed to Jonathan A. Baker (jonathan.baker@metoffice.gov.uk)